

Sheath folds as a strain gauge in simple shear

Marta Adamuszek^{*(1)}, Marcin Dabrowski^(1,2)

⁽¹⁾ Computational Geology Laboratory, Polish Geological Institute – National Research
Institute, Wrocław, Poland

⁽²⁾ Physics of Geological Processes, University of Oslo, 0316 Oslo, Norway

Abstract

We investigate initiation and evolution of sheath folds developing in multilayer sequences around slip surfaces in simple shear. The slip surface is initially circular and oriented at 135° to the shearing direction. The flow perturbation around the rotating and deforming slip surface initiates the growth of deflections of the layers, which serves as precursors for the sheath structure. The influence of the perturbed flow on the fold growth decreases with strain as the structure is moved away from the slip surface. For $\gamma > 10$, the sheath fold evolution is dominated by a passive simple shear.

We describe the fold geometry using: 1) interlimb angle (α), 2) hinge angle (β), and 3) aspect ratio of the eye-structures in the section normal to the shearing direction at the fold base (R_{yz}). We show that the fold shapes developing in different interfaces can be characterized by a unique combination of the three parameters depending on strain magnitude. We present three strain gauge diagrams, which can be used to decipher strain from sheath folds based on any combination of two out of three parameters (α , β , R_{yz}).

We approximate the late evolution of the modelled sheath folds by analysing the passive deformation of cone structures in simple shear. We show that R_{yz} is asymptotically proportional to the square root of strain magnitude.

Keywords (6): sheath folds, non-cylindrical folds, eye-structures, simple shear, cone shape, strain gauge

1. Introduction

Non-cylindrical fold structures, which are characterized by a sharp hinge line bend (hinge angle) of more than 90° are termed sheath folds (Ramsay and Huber, 1987). In sections normal to the fold elongation, they give rise to a characteristic eye-shaped pattern. The number of closed contours seen in each section depends on the relation between the position of the section, the size of the fold, and layer thickness (e.g., Reber et al., 2012). Alsop and Holdsworth (2006) used the quotient of the aspect ratios of the outermost and the innermost closed contour to develop sheath fold classification. The authors distinguished three types of folds: analogous-eye, cat's-eye, and bull's-eye, in which the ratio of the outermost closed contour is the same, smaller, and larger from the ratio of the innermost closed contour, respectively. Further, they related the three fold patterns to the corresponding types of bulk strain deformation: plane strain, flattening, and constrictional. Reber et al. (2013a) showed that the sheath fold classification based on the contour aspect ratios may lead to erroneous results and should be carefully used for bulk strain type interpretations. Similar concerns regarding genetic interpretations based on the sheath fold classification were expressed in the work of Marques et al. (2008).

Sheath folds are found in various rock types in a broad spectrum of geological settings across a wide range of scales (Alsop et al., 2007). However, it is generally recognized that they predominantly form during high strain deformation in a simple shear-dominated regime (Cobbold and Quinquis, 1980). Various mechanisms of sheath fold formation in simple shear have been suggested in the literature (Figure 1A). Passive amplification of a pre-existing dome-shaped layer interface perturbation is perhaps the most widespread model used to explain sheath fold development (Quinquis et al., 1978; Minnigh, 1979; Cobbold and Quinquis, 1980; Skjernaa, 1989; Mies, 1993). Approximating the initial layer interface perturbation as an upright cone, Mies (1993) used analytic geometry and graphical simulations to estimate shear strain based on 1) the aspect ratios of the contours, 2) the interlimb angle, and 3) the hinge angle (Figure 1B). Based on analogue experiments, Marques et al. (2008) showed that sheath folds can develop in perturbed layers with dissimilar viscosities of a ratio smaller than 10.

The other group of models explains sheath fold development by various perturbation mechanisms of the simple shear flow field such as 1) above a rigid corrugated basement (Cobbold and Quinquis, 1980), 2) around rigid inclusions (Marques and Cobbold, 1995; Rosas et al., 2002; Marques et al., 2008), and 3) around slip surfaces (Reber et al., 2012;

Reber et al., 2013a; Reber et al., 2013b). Cobbold and Quinquis (1980) studied theoretically and experimentally sheath fold evolution above the corrugated surface. The authors derived a two-dimensional analytical solution for the velocity field above a rigid layer with regularly spaced grooves. Rosas et al. (2002) demonstrated how a sheath fold can develop around a rotating rigid inclusion in a shear zone. The impact of various parameters such as the shape of the inclusion and the distance of the marker layer from the inclusion was analysed. The study allowed for indicating configurations that are less likely for the sheath folds to develop. A systematic study of sheath fold formation around a slip surface was performed by Reber et al. (2013a). A range of parameters including slip surface size and orientation, strain magnitude, layer thickness, and cross-section location were investigated in terms of their impact on the aspect ratio of the outermost and innermost contours and the sheath fold length. The three-dimensional analytical flow model allowed for analysis of the structure development in high resolution. The analysis was carried out on densely spaced yz-sections. The slip surface model was also positively tested for the case of a mechanically stratified matrix with viscosity ratio less than 50 between the layers using analogue experiments (Reber et al., 2013b).

Alsop and Holdsworth (2012) presented a natural multilayer sheath fold example with rheologically distinct layering. Based on a series of sections, the authors described a three-dimensional shape of the 11 interfaces constituting the structure. They showed that the aspect ratio of the closed contours is larger in folds with larger hinge and interlimb angles. Moreover, the aspect ratio increases towards the fold nose. Thus, following Alsop and Holdsworth (2006), the fold was classified as a cats-eye fold. The interlimb angle changes between 12 and 40 degrees, whereas the aspect ratio of the closed contour observed in the most distant sections for different interfaces varies between 4 and 5.6. According to the authors, the overall geometrical analysis suggests that the fold was developed during general shear deformation due to the amplification of an initial perturbation.

In this paper, we analyse the initiation and evolution of sheath folds that form around slip surfaces in simple shear. The aim of the work is to gain a more detailed insight into sheath fold evolution. Similarly to Reber et al. (2013a), we use the analytical Eshelby solution reduced to the case of an incompressible viscous medium and an inviscid elliptical inclusion (slip surface). However, in contrast to the previous work, we focus on the three-dimensional shape analysis of individual interfaces rather than the eye-shaped structures displaying on the yz section. The approach significantly reduces the complexity of the analysis and allows for a better control on the evolution of fold shape parameters. We use the

term sheath structure *sensu lato*, including all non-cylindrical folds exhibiting eye patterns in the yz section, without the hinge angle necessarily below 90° .

We show that the deformation of a right cone can be used to approximate the late shape evolution of the sheath fold in the slip surface model. We derive an analytical formula for the change of the aspect ratio of the outermost closed contour, the hinge angle, and the interlimb angle with strain. Finally, we present a strain gauge diagram based on a combination of two out of three parameters: 1) the aspect ratio of the outermost contour, 2) the hinge angle, and 3) the interlimb angle.

2. Mechanical Model

We study a three-dimensional mechanical model of sheath fold development around a slip surface in simple shear up to shear strain of $\gamma=30$. The slip surface is embedded in a homogeneous, isotropic, and linear viscous matrix. We use a Cartesian coordinate system xyz, with x parallel to the shear direction. The centre of a prescribed circular slip surface is located in the origin of the reference system. The slip surface is initially oriented at $\theta=135^\circ$ to the shearing direction, which corresponds to the mode I fracture orientation (Figure 2A). The spatial coordinates are normalized by the slip surface radius. Thus, the slip surface radius is equal to 1 and its maximum vertical extent is $z_0=0.707$. During deformation, the slip surface can passively deform (rotate and stretch) but it cannot propagate (Means, 1989). Due to the point symmetry, we analyse only the upper part of the model. We use nine planes of passive markers that are equally distributed above the slip surface and located at $z_0=0.8, 0.95, 1.1, 1.25, 1.4, 1.55, 1.7, 1.85$, and 2.0 to visualize the fold evolution. Since no mechanical layering is present in the model, the developing folds are passive sheath folds (e.g., Cobbold and Quinquis, 1980). The fold geometry in each interface is described using the interlimb (α) and hinge (β) angles. The interlimb angle is measured as the minimum acute angle between the fold limbs in the area, where the fold forms a sheath structure, whereas the hinge angle is measured as the minimum angle along the hinge line, where hinge line is a curve that joins points of the maximum curvature (Figure 1B). Additionally, we examine the development of flanking structures on the central xz-section and eye-shaped patterns on multiple yz-sections.

We track the evolution of interfaces by numerically integrating the velocity field around the slip surface with strain. The velocity field is obtained using a modified Eshelby solution (see Exner and Dabrowski, 2010 for details). In simulations, we use a 4th order Runge-Kutta scheme for time integration (e.g., Keller, 1993).

3. Results

3.1. Sheath fold structure

Figure 3 shows the side and top views of the four selected interfaces after $\gamma=30$, for which $z_0=0.8, 1.1, 1.4$, and 1.7 . The thick black lines indicate the positions of the yz section at the sheath structure base and the contour shapes are shown on the right side of the figure. The analysed interfaces form the outermost closed contour of the eye-pattern on the selected yz section.

The folds have notably different geometry and size depending on the interface. In the side view, we can distinguish a long upper limb and a short lower limb. The lower limb is inverted and has a nearly flat shape. The geometry of the upper limb is more complex due to local curvature changes resulting in a second subsidiary hinge zone. The fold appears to have an asymmetric box-shape with a straight segment between the hinges. The straight segment is longer for distant interfaces.

The length and orientation of the inverted limb controls the span along x-axis where the closed contours and thus the sheath structure *sensu lato* can be observed. The length of the inverted limb and, thus, the length of the sheath structure is smaller for distant interfaces. The interlimb angle increases for distant interfaces and is equal to $\alpha=2.3^\circ$ for $z_0=0.8$ and $\alpha=5.0^\circ$ for $z_0=1.7$ (note vertical exaggeration for the side view in Figure 3). The hinge angle (β) is the smallest for the lowermost interface and the largest for the most distant interface. For $z_0=0.8$, β is equal to 13° and for $z_0=1.7$ it is 53° . The closed contour aspect ratio (R_{yz}) is calculated as a ratio between the maximum extents of the closed contour measured in the horizontal and vertical directions. R_{yz} is higher for distant interfaces.

Figure 3 demonstrates the complexity of the sheath structure geometry. The fold outline observed in the top view shows a sine-shaped hinge line variation. The contour shapes in the yz section are asymmetric about the horizontal plane. The asymmetry is more pronounced for proximal interfaces, which exhibit pyramidal shapes with rounded corners. The more distant interfaces develop an almost elliptical geometry.

A small-scale sheath structure develops below the main sheath fold on the other side of the slip surface. In a yz cross-section, we would observe a double-eye fold (see Reber et al., 2012). In the current analysis, we focus on the structures that develop above the plane containing the slip surface.

We quantify the shape of the nine studied interfaces after $\gamma=30$ using four parameters: the fold height and length in the central xz section and the aspect ratio and asymmetry of the closed contours appearing on different yz sections (Figure 4). The fold height is measured as the distance between the topmost point on the fold interface and the initial interface plane. The fold length is calculated as a distance between the two most distant yz sections, in which the closed contours can be observed. The aspect ratio of the closed contour is measured for different yz sections and we use r_{yz} to differentiate it from the aspect ratio measured at the sheath structure base (R_{yz}). To quantify the degree of asymmetry, we split each closed contour into the lower and upper part dividing it by the line joining the left- and rightmost hinge points. The degree of asymmetry is defined as the ratio between the heights of the upper and lower parts of the contour. When the asymmetry coefficient is close to 1, the upper and lower part have equal heights and the contour is approximately mirror symmetric around the horizontal plane. For the analysed sheath structure, the asymmetry coefficient is always larger than 1.

The height and length of the sheath structure are larger in the proximal interfaces than in the distant ones (Figure 4A and B). The fold height is 5 times larger in the innermost interface $z_0=0.8$ than in the outermost interface $z_0=2.0$, whereas the fold length is more than an order of magnitude greater for $z_0=0.8$ than for $z_0=2.0$. Figure 4C and D shows the variation of the aspect ratio, r_{yz} , and the asymmetry of the closed contour along the x-axis for different interfaces. The aspect ratio r_{yz} is generally higher for distant interfaces and ranges between 6 and 11.5. For inner interfaces, r_{yz} variation is characterized by a local minimum along the length of the fold, whereas for the outer interfaces it decreases towards the apex. If we analyse sections at the fold base, we cut through the inner interface with smaller r_{yz} . Thus, we observe bull's-eye-folds. In sections away from the fold base, we can also find analogous-eyes and cat's-eyes.

The highest asymmetry is observed close to the fold base and gradually decreases towards the fold apex. The largest variation occurs in the proximal interfaces, e.g., for $z_0=0.8$, where it changes from 7.4 at the fold base to almost 1 at the apex. The eye patterns developing in distant interfaces are more symmetrical e.g., for $z_0=2.0$ the value is between 1.7 and nearly 1.

3.2. Interface shape evolution

We analyse the shape evolution of interfaces with strain. Figure 5 shows the intersections of interfaces in the central xz section ($y=0$) for selected strain values $\gamma=1, 5, 10, 20$, and 30 . A rapid rotation of the slip surface is observed in the initial stages of deformation. The orientation measured with respect to the shearing direction changes from the initial value of $\theta=135^\circ$ to $\theta=14^\circ$ for $\gamma=5$ and $\theta=6^\circ$ for $\gamma=10$. The angle approaches the asymptotic value of $\theta=0^\circ$ with further deformation. The length of the slip surface interception in the xz section (slip line) changes during deformation. Initially, it decreases attaining a minimum length at $\gamma=1$. Further deformation leads to elongation of the slip line. For $\gamma=10$, the aspect ratio of the slip surface is around 6, and for $\gamma=30$, it exceeds 20. The rotation of the slip surface promotes interface bending and asymmetric folding. Fold structures develop in the vicinity of both tips of the slip surface. The structures below and above the slip surface are point symmetric with respect to the centre of the slip surface. We focus our analysis on the regions above the slip surface.

We distinguish three evolving regions hosting different kinds of structures (Figure 5). The regions are bounded by the extrapolation of the slip line and separated by the vertical lines that intercept the slip line tips. The interfaces in region I are virtually undeformed. Only towards the triangular region III, we observe a narrow zone with slightly deflected interfaces. In region II, which extends above the slip surface, the interfaces form a gentle asymmetrical synform, with a steeper and longer right limb compared to the left limb (note the vertical exaggeration 5:1 in Figure 5). The interface deflections decrease away from the slip surface. Initially, the interface deflections grow and, at the same time, the synform is stretched. The initially rapid evolution of the deflections slows down with strain and the syncline becomes more gentle due to progressive stretching. In the part of the region close to the slip surface, the interfaces that are initially cut by the slip surface develop an antiformal structure. The antiform migrates towards region III, becoming the innermost, core part of the sheath fold structure. For $\gamma=5$, the boundary line between region II and III intercepts the fold hinge zone for all the interfaces. Folds developed in the proximal interfaces are tight, strongly asymmetric and their amplitudes are large. Folds developing in the distant interfaces are wider, more symmetrical and have smaller amplitudes. Although further deformation causes only a slight fold growth in the vertical direction, we observe a significant stretch of the hinge zone, rotation and eventually inversion of the right fold limb. The hinge zone located above the tip of the slip surface gets smoother, whereas the hinge zone that defines the apex of the

sheath structure sharpens. As a result, an asymmetric box fold forms in region III, which further transforms into a non-cylindrical fold structure and finally a sheath fold. The folds develop earlier in the proximal interfaces than in the distant ones. The position of the yz-section along the x-axis, in which any given interface forms the outermost closed contour is determined by the location of the rearmost (here leftmost) point of the inverted fold limb. The positions of such sections are found closer to the origin of the coordinate system in the proximal interfaces.

We show the evolution of the fold height, fold length, the outermost closed contour aspect ratio at the sheath structure base, and the closed contour asymmetry as a function of strain for the nine selected interfaces in Figure 6. The proximal interfaces develop closed contours earlier during deformation compared to the more distant interfaces. Closed contours can be found in the two innermost interfaces $z_0=0.8$ and 0.95 already for $\gamma=6$, whereas it requires $\gamma=24$ to develop closed contours in the $z_0=2.0$ interface.

The fold height is always the largest for $z_0=0.8$. For $\gamma=15$, it reaches ca. 0.55 and further deformation leads to only minor changes. The maximum fold height decreases for distant interfaces. The amount of strain required to reach the nearly maximum possible height is larger for outer interfaces. At each stage of deformation, the folds are longer in the proximal than in the distant interfaces. R_{yz} increases with strain for all interfaces and the value is always smaller in the proximal than distant interfaces. For $\gamma=15$, we observe closed contours in the six lowermost interfaces. Their aspect ratios R_{yz} vary between 5 and 6.5. For $\gamma=30$, closed contours are present in all the interfaces and their aspect ratio varies between 6.5 and 11.6. The asymmetry of the contours increases with strain. For $z_0=0.8$ it is equal to ca. 1.3 at $\gamma=6$ and 7.6 at $\gamma=30$. The asymmetry developed in the distant interfaces is always smaller than in the proximal ones.

3.3. Strain gauge diagrams

Dashed lines in Figure 7A and B show the evolution of R_{yz} for the nine interfaces as a function of the interlimb angle (α) and hinge angle (β), respectively, whereas, in Figure 7C, they illustrate a relation between α and β . Solid lines connect the values obtained for different interfaces for selected strain values $\gamma=10, 15, 20, 25$, and 30 . R_{yz} exhibits an approximate linear dependence on both α and β in the double-logarithmic plot. Similarly, a linear trend is observed in the α and β relation. R_{yz} increases and both α and β decrease with strain. For a given strain, R_{yz} , α , and β are always larger for distant interfaces. Hence, the fold shape can

be described uniquely using the three parameters for a given strain. However, it is sufficient to use two out of the three geometrical parameters to decipher the shear strain. Thus, the plots presented in Figure 7 can be used as strain gauge diagrams.

The grey field in Figure 7B and C delineates the area, where the hinge angle (β) is less than 90° and the non-cylindrical fold satisfy the sheath fold definition. During deformation, the folds that are initially characterized with a large hinge angle evolve into sheath fold *sensu stricto*. However, we can always find distant interfaces that are characterized by a wide hinge angle of more than 90° .

3.4. Analysis of the rate of deformation

In Figure 8, the isocontours show the deviation of the rate of deformation measured in the model (D) from the background rate of deformation (\bar{D}), where the rate of deformation is given by the symmetric part of the velocity gradient. The deviation is quantified using the second invariant of the difference between the two rate of deformation tensors $\tilde{D} = D - \bar{D}$. The blue and green contour lines indicate the values of \tilde{D} equal to 0.05 and 0.2, respectively, whereas the thick and thin grey lines show the selected interface shapes.

A zone of increased deformation localizes along the slip surface and shows a characteristic butterfly shape at the both slip surface tips. The shape of the zone evolves as the size and orientation of the slip surface changes. At the initial stages, shearing is localized close to the slip surface such that for $\gamma=1$ the $\tilde{D} = 0.05$ contours outline a narrow area and the $\tilde{D} = 0.2$ contours are almost undistinguishable (Figure 8A). Further deformation and the stretching of the slip surface cause that the zone is longer and wider and the butterfly shape is greater (Figure 8B). For $\gamma>10$, the two contours that outline the zone along the slip surface grow horizontally but do not expand vertically, whereas the size of the butterfly shape decreases (Figure 8C, D, and E).

At the initial stages of deformation, the perturbation of the interfaces is initiated and grows around the regions of high \tilde{D} (Figure 8A and B). However, already for $\gamma>10$, the perturbed interfaces move to the region ahead of the slip surface tip, where the background deformation dominates, and evolve into sheath folds. The influence of the slip surface on the sheath fold development is negligible for $\gamma>20$.

To estimate the role of passive deformation in sheath structure evolution, we compare the fold shape developed in the $z_0=0.8$ interface for $\gamma=9$ (G9) with the fold shapes that are generated in the same interface for larger strains $\gamma=15$ (G15) and $\gamma=21$ (G21). The two latter

287 folds are subject to a passive simple shear backward deformation of $\gamma=-6$ and $\gamma=-12$
 288 respectively, such that the three models illustrate the fold shape for effectively the same strain
 289 of $\gamma=9$. The contour plots in Figure 9A show the top view of the elevation of the structure for
 290 the three folds and the two dashed lines mark the position of the yz and the central xz sections,
 291 which are shown in Figure 9B and C, respectively.

292 The three structures exhibit similar shapes in the region past the slip surface tip
 293 (Figure 9C). The shape of the inverted fold limb and the fold apex are almost identical in the
 294 three models. A small discrepancy is noticeable in the upper fold limb, close to the sheath
 295 structure base, where the interface in the actual G9 model plunges slightly below the upper
 296 limbs of the retrodeformed folds. As a result, we observe a small misfit between the shapes of
 297 the closed contours in Figure 9B. The straight segment of the upper limb is the longest in G21.
 298 The significantly different shape of the upper limb is the main reason of the discrepancy
 299 between the three fold shapes observable in Figure 9A and Figure 9B.

300 4. Passive deformation model of the sheath fold evolution

301 To develop a passive deformation model of the sheath structure evolution for large
 302 strains, we approximate the fold shape with a right circular cone structure with an initial
 303 opening angle α_0 . The cone is inclined to be horizontal along the slant height. We analyse the
 304 cone shape evolution during progressive simple shear and measure: 1) the aspect ratio of the
 305 contour in the yz sections (R_{yz}), 2) the cone angle in the central xz plane that bisects the cone
 306 in the centre (α), which is analogous to the interlimb angle and 3) the angle in the plane
 307 normal to the xz plane that also bisects the cone in the centre (β), which is analogous to the
 308 hinge angle (Figure 10).

309 The cone intercepts with a reference vertical section giving an ellipse (the black line
 310 in Figure 10). The lengths of the horizontal and vertical axes of the ellipse are denoted by R_y
 311 and R_z , respectively. In the analysis, we set the origin of the coordinate system in the
 312 lowermost point of the reference ellipse (the black dot in Figure 10). The aspect ratio of the
 313 ellipse is given by (see Appendix A)

$$314 \quad R_{yz} = \frac{\sqrt{\cos(\alpha_0)}}{\cos\left(\frac{\alpha_0}{2}\right)} \quad (1)$$

315 The aspect ratio of the ellipse increases with strain. The length of the vertical axis
 316 remains the same ($R'_z = R_z$), whereas the length of the horizontal axis (R'_y) is inherited from

an ellipse embedded in a cone section inclined at an angle φ to the reference vertical section (the white contour in Figure 10). The angle is related to shear strain γ through $\varphi = \tan^{-1} \gamma$. The ellipse aspect ratio R_{yz} changes with strain as (see Appendix B):

$$R_{yz} = \frac{\sqrt{\gamma \sin(\alpha_0) + \cos(\alpha_0)}}{\cos\left(\frac{\alpha_0}{2}\right)} \quad (2)$$

For the initially elliptical cone shape, (see Appendix C), we obtain

$$R_{yz} = f \frac{\sqrt{\gamma \sin(\alpha_0) + \cos(\alpha_0)}}{\cos\left(\frac{\alpha_0}{2}\right)} \quad (3)$$

where f denotes the initial cone aspect ratio. Note that Eq. (2) and (3) differ only by the factor f , which indicates that the initial flattening of the cone does not influence the scaling between R_{yz} and α_0 .

The evolution of the cone angles α and β with strain are given by the following expressions (Appendix D)

$$\alpha = \tan^{-1} \left[\frac{\sin(\alpha_0)}{\gamma \sin(\alpha_0) + \cos(\alpha_0)} \right] \quad (4)$$

and

$$\beta = 2 \tan^{-1} \left[R_{yz} \frac{\sin\left(\frac{\alpha}{2}\right)}{\sqrt{\cos(\alpha)}} \right] \quad (5)$$

Note that we have simplified the expression for β by deriving it as a function of α and not α_0 .

Figure 11 shows the evolution of R_{yz} , α , and β with strain obtained using the analytical expressions (Eq. (2), Eq. (4), and Eq. (5)) for α_0 varying between 10 and 170 together with the simulation results for the nine analysed interfaces. The analytical expression for R_{yz} gives an exact linear trend with strain in the double-logarithmic plot only for $\alpha_0=90$

$$R_{yz} = \sqrt{2\gamma} \quad (6)$$

For $\alpha_0 \neq 90^\circ$, the relation is visibly non-linear with strain for small strain and almost linear for larger strain. The contribution of the $\cos(\alpha_0)$ term in the nominator in Eq. (2) decreases with strain and for larger strains the expression can be approximated with

$$R_{yz} \approx c(\alpha_0) \sqrt{\gamma} \quad (7)$$

where c is a constant dependent on the initial cone angle. In the case of an elliptical cone shape, the slope does not change but it will be shifted upwards or downwards by a factor f (Appendix C). The simulation results for all analysed interfaces (Figure 11B) show a similar trend to the one observed for the right cone.

The analytical expression for α is also non-linear for small strains and becomes nearly linear with strain (Figure 11C). It can be approximated with a relation

$$\alpha \approx c(\alpha_0) \frac{1}{\gamma} \quad (8)$$

The curves are convex for $\alpha_0 < 90^\circ$ and concave for $\alpha_0 > 90^\circ$. For the case of $\alpha_0 = 90^\circ$, Eq. (4) reduces to

$$\alpha = \tan^{-1} \frac{1}{\gamma} \quad (9)$$

The relations shown for the numerical results have concave shape characteristics similar to the analytically derived solution for large $\alpha_0 > 160^\circ$ (cf. Figure 11C and D).

The analytical solution for the evolution of β with strain shows approximately linear relation in the double-logarithmic plot for all α_0 , whereas the numerical results exhibit slightly curved lines for all interfaces (cf. Figure 11E and F). However, the curves shown in the two plots are characterized by distinctly different slopes in the log-log axis.

5. Discussion

5.1. Sheath fold geometry

Sheath folds are commonly described as structures with either conical (e.g., Ramsay, 1958) or paraboloidal (e.g., Carey, 1962) shape. However, we show that sheath folds may exhibit a more complex geometry. In the yz section, the simulated sheath folds at their base show strongly asymmetrical, pyramidal contours with rounded corners, whereas the contours are more elliptical at the apex (Figure 3). In the multilayer sequence, each interface is characterized by a distinct set of geometrical parameters such as interlimb angle (α), hinge

angle (β), and aspect ratio of the outermost closed contour (R_{yz}). A single parameter is not sufficient to uniquely describe the interface (Figure 7). Due to a large variation in the shape of individual interfaces, the description of the multilayer sequence is a challenging task. Moreover, the classification of such a structure as sheath fold might be problematic, where e.g. only some layers have a hinge angle below 90° and can be classified as sheath folds *sensu stricto* (see Figure 7B).

Based on serial sectioning of a natural example of a multilayer sheath structure, Alsop and Holdsworth (2012) depicted it as a self-similar structure and argued that the bulk three-dimensional fold geometry can be reproduced from the analysis of a single yz section. In this study, sheath folds exhibit higher R_{yz} in the proximal than in the distant interfaces and the increase of R_{yz} is correlated with an increase of α and β . Alsop and Holdsworth (2012) concluded that the fold was formed due to the amplification of the initial layer perturbation in general shear, and the viscous layering played a key role during deformation. Since we describe the sheath structure development due to flow perturbation around a slip surface embedded in a homogeneous rock matrix, the difference in the fold shapes can be attributed to both the different mechanisms of the fold formation and the mechanical role of the layers. Additionally, some discrepancy between observations can be related to the difference in the orientation of the yz-sections. Alsop and Holdsworth (2012) analysed the yz-sections oriented normal to the fold elongation, whereas we orient them normal to the shearing direction. In our opinion, the shearing direction, which in the case of simple shear deformation coincides with orientation of lineation and foliation, is easier to establish accurately in the field than the fold elongation, especially when the analysed fold is not exposed in three-dimensions. For large deformation, the folds are oriented subhorizontally and the difference between different approaches of defining the yz sections diminishes.

In our fold shape analysis, we choose to analyse the closed contours in each interface in the yz-section located at the fold base. The analysed interfaces form the outermost closed contour in such sections. The outermost closed contour is one of the most distinct features of the fold and it is generally easy to measure in the field. The same parameter has been used in the sheath fold classification by Alsop and Holdsworth (2006) and the detailed sheath fold analysis by Reber et al. (2012). The results of the R_{yz} analysis presented in the study are consistent with the results presented in the work of Reber et al. (2013a).

5.2. Evolution of the sheath structures

During initial stages of deformation, the flow perturbation around rotating slip surface leads to development of the interface deflections near the slip surface tip, which are a trigger for the sheath structure development. Due to shearing, the sheath structure starts to develop ahead of the slip surface and it is accompanied by the formation of a synformal structure directly above the slip surface. Since the interfaces away from the fold and synformal structures are nearly undeformed, the fold growth must be balanced by the growth of the synform. Formation of the two structures was also described by Adamuszek et al. (2016), for sheath folds developing around layer-parallel slip surfaces.

For $\gamma > 10$, the evolution of the sheath structure is dominated by the passive simple shear deformation and is practically independent from the flow perturbation around the slip surface. Hence, the late evolution of the fold geometry can be easily obtained for an arbitrary strain by subjecting the fold to the simple shear deformation.

5.3. Strain map

The shape of each interface at different deformation stages can be uniquely described using the hinge angle α , the interlimb angle β , and the aspect ratio of the outermost closed contour R_{yz} . This gives a potential tool to decipher strain from the fold geometry. We show that two shape parameters are necessary to close the relation. We provide three strain gauge diagrams that relate strain magnitude to R_{yz} and α , R_{yz} and β , or α and β (Figure 7).

The diagrams illustrate that single geometrical parameter is not sufficient to determine strain and some generalizations can lead to erroneous interpretations e.g., large interlimb angle is not diagnostic for small strain values. For some cases, the diagrams can be used to obtain constraints on the strain magnitude value e.g., $R_{yz}=10$ indicates $\gamma > 25$.

The diagrams are constructed based on the analysis of the folds developed for a specific initial geometry and boundary conditions. However, based on the analysis provided by Reber et al. (2012), we expect that the gauge diagrams would look differently for models with e.g. different shape and orientation of the slip surface. The analysis of sensitivity of an additional factor on the set of three parameters could be a potential tool to gain more information about deformation or initial conditions. Since the exposures of natural sheath structures rarely allow obtaining the three geometrical parameters, we limited the analysis to two parameters and assumed a slip surface geometry and conditions that seem to be most likely to occur in nature in simple shear deformation regime.

Detailed field measurements of sheath folds such as presented by Alsop and Holdsworth (2012) can be used to estimate strain magnitude. According to our model, the obtained values of α varying between 12 and 40 degrees and R_{yz} varying between 4 and 5.6 correspond to shear strains between 8 and 15. However, neglecting effects due to the coaxial component of deformation and viscosity differences between the layers may not be justified in this case.

5.4. Cone shape

Despite the complex geometry of the sheath structure, we used a right cone to approximate the fold shape and analyse how it deforms during simple shear. The approximate model can be only applied to the passive stage of the sheath fold evolution, away from the slip surface, so generally for $\gamma > 10$. Both the numerical simulations and the analytical solution show that R_{yz} scales with $\sqrt{\gamma}$ for large strain. Since in the analytical solution, we consider the cone with a circular base, and the simulation results and the analytical solution are not exactly the same. If we use an elliptical cone shape, we obtain the scaling that allows matching the two curves. Using the initial cone angle $\alpha_0 > 160^\circ$, we could also reproduce the correlation between α and γ . However, we could not obtain the exact scaling between β and γ . This could be attributed to the simplification of the sheath structure while using the cone shape. In the analytical solution, the hinge line variation is approximated with two half-lines originating at the cone apex, whereas the results of the simulation show a sine-shaped hinge line variation (top view of structure in Figure 3).

The deformation of the right cone shape to approximate the sheath fold development was also studied by Skjernaa (1989) and Mies (1993). However, the authors examined the fold evolution during passive amplification of the pre-existing perturbation and they used a differently oriented cone. Thus, the results of their analysis are significantly different to those presented in the study.

6. Conclusions

1. The flow perturbation around rotating and deforming slip surfaces in simple shear causes interface deflections, which are precursors of the sheath structure.
2. Progressive deformation moves the developing sheath fold away from the slip surface into the regions, where passive simple shear dominates. For shear strain $\gamma > 10$, passive deformation controls the sheath structure evolution.

3. Each interface of the sheath fold structure has a unique shape at a given strain. We present three strain gauge diagrams that allow using two out of three parameters 1) the aspect ratio of the outermost closed contour, 2) the hinge angle, and 3) the interlimb angle to estimate the shear strain.
4. For large strains, the fold shape evolution can be approximated by the deformation of a horizontally oriented cone shape. We developed an analytical expression that describes the evolution of the aspect ratio of the outermost closed contour, the interlimb angle, and the hinge angle. Due to the simplification of the fold geometry, noticeable differences in the evolution of these parameters between analytical solution and numerical result are recorded only for the hinge angle.

7. Acknowledgements

We acknowledge the funding by the National Science Centre, based on the decision number DEC-2013/11/D/ST10/03458, and the Polish Geological Institute research project no. 61.9015.1601.00.0.

8. References

- Adamuszek, M., Burliga, S., Dabrowski, M., 2016. Evolution of sheath folds around layer-parallel slip surfaces: *Salt Review* 12, 42–50.
- Alsop, G. I., Holdsworth, R. E., 2006. Sheath folds as discriminators of bulk strain type: *Journal of Structural Geology* 28 (9), 1588-1606.
- Alsop, G.I., Holdsworth, R.E., McCaffrey, K.J.W., 2007. Scale invariant sheath folds in salt, sediments and shear zones. *Journal of Structural Geology* 29, 1585–1604.
- Alsop, G. I., Holdsworth, R. E., 2012. The three dimensional shape and localisation of deformation within multilayer sheath folds: *Journal of Structural Geology* 44, 110-128.
- Carey, S. W., 1962. Folding: *J. Alberta Soc. Petrol. Geol.* 10, 95-144.
- Cobbold, P. R., and Quinquis, H., 1980. Development of Sheath Folds in Shear Regimes: *Journal of Structural Geology* 2 (1-2), 119-126.
- Exner, U., Dabrowski, M., 2010. Monoclinic and triclinic 3D flanking structures around elliptical cracks: *Journal of Structural Geology* 32 (12), 2009-2021.
- Keller, H.B., 1993. *Numerical Methods for Two-point Boundary-value Problems*. Dover Publications.
- Marques, F. G., Cobbold, P. R., 1995. Development of Highly Noncylindrical Folds around Rigid Ellipsoidal Inclusions in Bulk Simple Shear Regimes - Natural Examples and Experimental Modeling: *Journal of Structural Geology* 17 (4), 589-&.
- Marques, F. O., Guerreiro, S. M., and Fernandes, A. R., 2008. Sheath fold development with viscosity contrast: Analogue experiments in bulk simple shear: *Journal of Structural Geology* 30 (11), 1348-1353.
- Means, W. D., 1989. Stretching Faults: *Geology* 17 (10), 893-896.

- Mies, J. W., 1993. Structural-Analysis of Sheath Folds in the Sylacauga-Marble-Group, Talladega Slate Belt, Southern Appalachians: *Journal of Structural Geology* 15 (8), 983-993.
- Minnigh, L. D., 1979. Structural-Analysis of Sheath-Folds in a Meta-Chert from the Western Italian Alps: *Journal of Structural Geology* 1 (4), 275-282.
- Quinquis, H., Audren, C., Brun, J. P., Cobbold, P. R., 1978. Intense Progressive Shear in Ile De Groix Blueschists and Compatibility with Subduction or Obduction: *Nature* 273 (5657), 43-45.
- Ramsay, J. G., 1958. Superimposed folding at Loch Monar, Inverness-shire and Ross-shire: *Quart. Jour. Geol. Soc. London* 113, 271-307.
- Ramsay, J. G., Huber, M. I., 1987. The techniques of modern structural geology. Volume 2: Folds and fractures, London; New York, Academic Press.
- Reber, J. E., Dabrowski, M., Galland, O., Schmid, D. W., 2013a. Sheath fold morphology in simple shear: *Journal of Structural Geology* 53, 15-26.
- Reber, J. E., Dabrowski, M., Schmid, D. W., 2012. Sheath fold formation around slip surfaces: *Terra Nova* 24 (5), 417-421.
- Reber, J. E., Galland, O., Cobbold, P. R., de Veslud, C. L., 2013b. Experimental study of sheath fold development around a weak inclusion in a mechanically layered matrix: *Tectonophysics* 586, 130-144.
- Rosas, F., Marques, F. O., Luz, A., Coelho, S., 2002. Sheath folds formed by drag induced by rotation of rigid inclusions in viscous simple shear flow: nature and experiment: *Journal of Structural Geology* 24 (1), 45-55.
- Skjernaa, L., 1989. Tubular Folds and Sheath Folds - Definitions and Conceptual Models for Their Development, with Examples from the Grapesvare Area, Northern Sweden: *Journal of Structural Geology* 11 (6), 689-703.

Figure captions

Figure 1 A) Models of sheath fold formation in simple shear: passive amplification of a pre-existing perturbation, flow perturbation above a corrugated rigid basement, flow perturbation around a rigid inclusion, and flow perturbation around a slip surface (weak inclusion) (modified after Cobbold and Quinquis, 1980). B) 3-dimensional sketch illustrating interlimb angle (α), hinge angle (β), and aspect ratio of the outermost closed contour (R_{yz}) of a sheath fold.

Figure 2. Schematic illustration of the model geometry in the xz section showing the slip surface and the analysed interfaces. The model is subject to simple shear deformation that acts in x direction. The slip surface is oriented at $\theta=135^\circ$ to the shearing direction.

Figure 3 Side (xz) and a top (xy) view of the fold shapes for selected interfaces after $\gamma=30$ for A) $z_0=0.8$, B) $z_0=1.1$, C) $z_0=1.4$, and D) $z_0=1.7$. Dotted white lines in the side view show the hinge line of the structure. α and β indicate the interlimb and hinge angle, respectively. Note that vertical exaggeration in the side view is 5:1. The black thick line shows the locations of the outermost contour, which are presented in the yz view (the yz view is in scale). R_{yz} denotes the aspect ratio of the outermost closed contour.

Figure 4 A) Fold height and B) fold length for different interfaces. Variation of C) the aspect ratio (r_{yz}) and D) asymmetry of the closed contour along the x-axis. The results are presented for $\gamma=30$. Star markers in C) and D) refer to the fold geometry presented in Figure 3.

Figure 5 The central xz section for A) $\gamma=1$, B) $\gamma=5$, C) $\gamma=10$, D) $\gamma=20$, and E) $\gamma=30$. Selected interfaces are marked with thick lines ($z_0=\pm 0.8, 1.1, 1.4, 1.7$). Dashed lines separate three distinct regions of deformation: I – undeformed or slightly deformed, II – forming basin or dome structures, III – forming the sheath structure. The orientation of the slip surface (θ) is indicated in the right lower corner. Note the vertical exaggeration of 5:1.

Figure 6 A) Fold height, B) fold length, and C) aspect ratio (R_{yz}) and D) asymmetry of the outermost closed contour presented as a function of strain (γ) for nine different interfaces.

Figure 7 Aspect ratio of the outermost contour (R_{yz}) as a function of A) interlimb angle (α) and B) hinge angle (β). Solid lines show the simulation results for different interfaces and dashed lines join the points of the same strain. The grey field in B) indicates the area of sheath folds *sensu stricto*.

Figure 8 Colourmap illustrating the second invariant of the difference between the rate of deformation measured in the model and in the background for $\gamma=1, 5, 10, 20$, and 30 . The blue and green contour lines mark 0.05 and 0.2 contour values, respectively. Grey lines show the interface shape. For selected interfaces $z_0=\pm 0.8, 1.1, 1.4, 1.7$, and 2.0 , we use a thick line. Note that vertical exaggeration is $5:1$.

Figure 9 A) Top view of the $z_0=0.8$ interface for three cases: at $\gamma=9$, at $\gamma=15$ subjected to passive backward deformation of $\gamma=-6$, and at $\gamma=21$ subjected to passive backward deformation of $\gamma=-12$. Black dashed lines indicate the yz and xz cross-section positions, which are shown in B) and C), respectively.

Figure 10 Circular cone shape with initial opening angle α_0 used to approximate sheath structure evolution. α and β denote the cone angles measured during deformation in the two orthogonal planes that intersect along the cone axis. The thick black ellipse is a contour of a cone intersection with a vertical section. R_y and R_z denote the horizontal and vertical axis, respectively. The thick white line is an intersection of the cone with an inclined section, which contains the lowermost point (red dot) of the black ellipse. R'_y and R'_z denote the two axes of the white ellipse. The white ellipse corresponds to the location of the black ellipse prior to a certain amount of simple shear. A) shows the cone structure and the contours in a three-dimensional perspective whereas B) and C) are the side xz and yz views, respectively.

Figure 11 Evolution of A) and B) contour aspect ratio, C) and D) interlimb angle, and E) and F) hinge angle with strain. The plots on the left show the analytical solution for different initial cone angles (α_0) varying between 10 and 170 degrees, whereas the plots on the right illustrate simulation results for the outermost contour for the nine analysed interfaces.

Figure A1 Cone shape illustrating a simplified model of a sheath fold. Dark red line shows the cone axes, whereas the black line shows a contour of a vertical section through the cone. Red line illustrates a contour through the cone normal to the cone axis. See text for details.

Figure A2 Three-dimensional model of the initial cone shape that is used for the approximation of the initial sheath fold shape. Black line shows the contour of the initial section through the cone normal to the slant height, whereas the white line illustrates the contour at the angle φ . A) shows a 3D perspective and B) and C) show side and top views of the cone, respectively. See text for details.

Figure A3 A three-dimensional model of the deformed cone shape. White line illustrates the contour that was initially at the angle φ (see Figure A2). Red line is an axillary contour showing the section through the cone normal to the cone axis. A) shows a 3D perspective and B) and C) show side and top view of the cone, respectively. See text for details.

Appendix: Evolution of a cone shape in simple shear.

A. Ellipse ratio for the initial section

We derive the aspect ratio of the ellipse on a vertical section, which cuts the cone with the initial opening angle α_0 at A at the right angle (black contour). The vertical ellipse axis R_z is half of the \overline{AB} segment and it can be easily found in the xz section (Figure A1B), where $\overline{AB} = \overline{AO} \cdot \tan(\alpha_0)$, thus

$$R_z = \frac{\overline{AO}}{2} \tan(\alpha_0) \quad (10)$$

In order to determine the horizontal ellipse axis R_y , we construct an axillary section through the cone, which is oriented normal to the cone axis and intersects the vertical section along R_y axis (red contour). The axillary section gives a circle with a radius r . We find R_y using the Pythagoras theorem in the right triangle MCE (see Figure A1C), where the segment \overline{CE} is R_y of an ellipse and \overline{ME} is the circle radius r , thus

$$R_y = \sqrt{r^2 - \overline{MC}^2} \quad (11)$$

We define \overline{MC} as the difference between two segments (see Figure A1B)

$$\overline{MC} = \overline{KC} - r \quad (12)$$

and use it in Eq. (11)

$$\begin{aligned} R_y &= \sqrt{r^2 - (\overline{KC} - r)^2} = \sqrt{2 \cdot \overline{KC} \cdot r - \overline{KC}^2} = \\ &= \sqrt{\overline{KC}^2 \left(\frac{2 \cdot r}{\overline{KC}} - 1 \right)} = \overline{KC} \sqrt{\frac{2 \cdot r}{\overline{KC}} - 1} \end{aligned} \quad (13)$$

Next, we find \overline{KC} as (see Figure A1B):

$$\overline{KC} = \frac{R_z}{\cos\left(\frac{\alpha_0}{2}\right)} = \frac{\overline{AO}}{2} \cdot \frac{\tan(\alpha_0)}{\cos\left(\frac{\alpha_0}{2}\right)} \quad (14)$$

and derive r using the relation (see Figure A1B)

$$r = \overline{KM} = \overline{KO} \cdot \sin\left(\frac{\alpha_0}{2}\right) \quad (15)$$

Using the fact that

$$\overline{KO} = \frac{\overline{AO} + \overline{BO}}{2} \quad (16)$$

and that

$$\overline{BO} = \frac{\overline{AO}}{\cos(\alpha_0)} \quad (17)$$

we obtain

$$r = \frac{\overline{AO}}{2} \cdot \left[1 + \frac{1}{\cos(\alpha_0)} \right] \cdot \sin\left(\frac{\alpha_0}{2}\right) = \frac{\overline{AO}}{2} \cdot \frac{1 + \cos(\alpha_0)}{\cos(\alpha_0)} \cdot \sin\left(\frac{\alpha_0}{2}\right) \quad (18)$$

We rearrange Eq. (18) using the half angle formula, where $\cos^2(\alpha_0/2) = [1 + \cos(\alpha_0)]/2$ and further the double angle formula, where $\sin(\alpha_0) = 2 \sin(\alpha_0/2) \cos(\alpha_0/2)$ and get

$$r = \overline{AO} \cdot \frac{\cos^2\left(\frac{\alpha_0}{2}\right)}{\cos(\alpha_0)} \cdot \sin\left(\frac{\alpha_0}{2}\right) = \frac{\overline{AO}}{2} \cdot \frac{\cos\left(\frac{\alpha_0}{2}\right)}{\cos(\alpha_0)} \cdot \sin(\alpha_0) = \frac{\overline{AO}}{2} \cdot \cos\left(\frac{\alpha_0}{2}\right) \cdot \tan(\alpha_0) \quad (19)$$

We expand the part under the square root in Eq. (13) using Eq. (14) and Eq. (19), and simplify it

$$\frac{2 \cdot r}{\overline{KC}} - 1 = \frac{2 \cdot \frac{\overline{AO}}{2} \cdot \cos\left(\frac{\alpha_0}{2}\right) \cdot \tan(\alpha_0)}{\frac{\overline{AO}}{2} \cdot \frac{\tan(\alpha_0)}{\cos\left(\frac{\alpha_0}{2}\right)}} - 1 = 2 \cos^2\left(\frac{\alpha_0}{2}\right) - 1 = \cos(\alpha_0) \quad (20)$$

Substituting Eq. (20) and Eq. (14) into Eq. (13), the horizontal ellipse axis is given by

$$R_y = \frac{\overline{AO}}{2} \cdot \frac{\tan(\alpha_0)}{\cos\left(\frac{\alpha_0}{2}\right)} \sqrt{\cos(\alpha_0)} \quad (21)$$

Finally, we calculate the elliptical ratio (R_{yz}) using Eq. (21) and Eq. (10), thus

$$R_{yz} = \frac{R_y}{R_z} = \frac{\frac{\overline{AO}}{2} \cdot \tan(\alpha_0) \cdot \frac{\sqrt{\cos(\alpha_0)}}{\cos\left(\frac{\alpha_0}{2}\right)}}{\frac{\overline{AO}}{2} \cdot \tan(\alpha_0)} = \frac{\sqrt{\cos(\alpha_0)}}{\cos\left(\frac{\alpha_0}{2}\right)} \quad (22)$$

B. Ellipse ratio of the deformed cone

Now, we derive the vertical and horizontal ellipse axes of an ellipse R'_z and R'_y , accordingly, as a function of φ , which represent different section orientation with respect to the vertical direction. The relation between φ and γ is given by

$$\gamma = \tan(\varphi) \quad (23)$$

The vertical ellipse axis R'_z is represented by half of the segment PB segment and it can be derived from the relations visible in the xz section (Figure A2B).

$$R'_z = \frac{R_z}{\cos(\varphi)} = \frac{\overline{AO}}{2} \cdot \frac{\tan(\alpha_0)}{\cos(\varphi)} \quad (24)$$

R'_y is found from the relations visible in Figure A2C using the Pythagoras theorem in the triangle TEM:

$$R'_y = \sqrt{r^2 - \overline{ME}^2} \quad (25)$$

We find \overline{ME} as the difference between two segments $\overline{ME} = r - \overline{KE}$ (Figure A2B), thus

$$\begin{aligned} R'_y &= \sqrt{r^2 - \overline{ME}^2} = \sqrt{r^2 - (r - \overline{KE})^2} = \sqrt{2 \cdot \overline{KE} \cdot r - \overline{KE}^2} = \\ &= \sqrt{\overline{KE}^2 \left(\frac{2 \cdot r}{\overline{KE}} - 1 \right)} = \overline{KE} \sqrt{\frac{2 \cdot r}{\overline{KE}} - 1} \end{aligned} \quad (26)$$

To get \overline{KE} , we use law of sines in the triangle KEP and obtain a relation

$$\frac{\overline{KE}}{\sin(90 - \varphi)} = \frac{R'_z}{\sin\left(90 + \frac{\alpha_0}{2}\right)} \quad (27)$$

which we rearrange and simplify

$$\overline{KE} = R'_z \frac{\sin(90 - \varphi)}{\sin\left(90 + \frac{\alpha_0}{2}\right)} = R'_z \frac{\cos(\varphi)}{\cos\left(\frac{\alpha_0}{2}\right)} \quad (28)$$

Substituting R'_z from Eq. (24), we obtain

$$\overline{KE} = \frac{\overline{AO}}{2} \cdot \frac{\tan(\alpha_0)}{\cos(\varphi)} \cdot \frac{\cos(\varphi)}{\cos\left(\frac{\alpha_0}{2}\right)} = \frac{\overline{AO}}{2} \cdot \frac{\tan(\alpha_0)}{\cos\left(\frac{\alpha_0}{2}\right)} \quad (29)$$

Next, we derive r from relation (Figure A2B)

$$r = \overline{KM} = \overline{KO} \cdot \sin\left(\frac{\alpha_0}{2}\right) \quad (30)$$

where

$$\overline{KO} = \frac{\overline{PO} + \overline{BO}}{2} \quad (31)$$

\overline{PO} is defined as

$$\overline{PO} = \overline{PA} + \overline{AO} \quad (32)$$

where

$$\overline{PA} = 2R_z \cdot \tan(\varphi) = 2R_z \cdot \gamma \quad (33)$$

We get R'_z from Eq. (24) and substitute Eq. (33) into Eq. (32)

$$\overline{PO} = 2 \frac{\overline{AO}}{2} \cdot \tan(\alpha_0) \cdot \gamma + \overline{AO} = \overline{AO} [\gamma \cdot \tan(\alpha_0) + 1] \quad (34)$$

We expand Eq. (31) using Eq. (34) and Eq. (17)

$$\overline{KO} = \frac{\overline{AO} (\gamma \tan(\alpha_0) + 1) + \frac{\overline{AO}}{\cos(\alpha_0)}}{2} = \frac{\overline{AO}}{2} \left[\gamma \tan(\alpha_0) + \frac{1 + \cos(\alpha_0)}{\cos(\alpha_0)} \right] \quad (35)$$

Using the half angle formula for the cosine function, we get

$$\overline{KO} = \frac{\overline{AO}}{2} \left[\gamma \tan(\alpha_0) + \frac{2 \cos^2\left(\frac{\alpha_0}{2}\right)}{\cos(\alpha_0)} \right] \quad (36)$$

We substitute Eq. (36) into Eq. (30)

$$r = \frac{\overline{AO}}{2} \left[\gamma \tan(\alpha_0) + \frac{2 \cos^2\left(\frac{\alpha_0}{2}\right)}{\cos(\alpha_0)} \right] \sin\left(\frac{\alpha_0}{2}\right) \quad (37)$$

and modify it using the formula for double angles for the sine function

682

$$r = \frac{\overline{AO}}{2} \left[\gamma \tan(\alpha_0) \sin\left(\frac{\alpha_0}{2}\right) + \frac{\cos\left(\frac{\alpha_0}{2}\right) \sin(\alpha_0)}{\cos(\alpha_0)} \right] = \frac{\overline{AO}}{2} \tan(\alpha_0) \left[\gamma \sin\left(\frac{\alpha_0}{2}\right) + \cos\left(\frac{\alpha_0}{2}\right) \right] \quad (38)$$

684

We expand the part under the square root in Eq. (26)

$$\begin{aligned} \frac{2 \cdot r}{KE} - 1 &= \frac{2 \cdot \frac{\overline{AO}}{2} \tan(\alpha_0) \left[\gamma \sin\left(\frac{\alpha_0}{2}\right) + \cos\left(\frac{\alpha_0}{2}\right) \right]}{\frac{\overline{AO}}{2} \cdot \frac{\tan(\alpha_0)}{\cos\left(\frac{\alpha_0}{2}\right)}} - 1 = \\ &= 2 \left[\gamma \sin\left(\frac{\alpha_0}{2}\right) + \cos\left(\frac{\alpha_0}{2}\right) \right] \cos\left(\frac{\alpha_0}{2}\right) - 1 \end{aligned} \quad (39)$$

686 and simplify it

$$\frac{2 \cdot r}{KE} - 1 = 2\gamma \sin\left(\frac{\alpha_0}{2}\right) \cos\left(\frac{\alpha_0}{2}\right) + 2 \cos^2\left(\frac{\alpha_0}{2}\right) - 1 = \gamma \sin(\alpha_0) + \cos(\alpha_0) \quad (40)$$

688

Substituting Eq. (40) and Eq. (29) into Eq. (26), we obtain

$$R'_y = \frac{\overline{AO}}{2} \cdot \frac{\tan(\alpha_0)}{\cos\left(\frac{\alpha_0}{2}\right)} \sqrt{\gamma \sin(\alpha_0) + \cos(\alpha_0)} \quad (41)$$

690

Therefore, the axial ratio of the tilted ellipse with respect to the initial cone shape is

691 given by

$$\frac{R'_y}{R'_z} = \frac{\frac{\overline{AO}}{2} \cdot \frac{\tan(\alpha_0)}{\cos\left(\frac{\alpha_0}{2}\right)} \sqrt{\gamma \sin(\alpha_0) + \cos(\alpha_0)}}{\frac{\overline{AO}}{2} \cdot \frac{\tan(\alpha_0)}{\cos(\varphi)}} = \cos(\varphi) \frac{\sqrt{\gamma \sin(\alpha_0) + \cos(\alpha_0)}}{\cos\left(\frac{\alpha_0}{2}\right)} \quad (42)$$

693

However, if we take the fact that R'_z after deformation becomes R_z (Eq. (10)), the

694 equation showing an evolution of the cone shape visible on the section has the form

$$\frac{R'_y}{R_z} = \frac{\frac{\overline{AO}}{2} \cdot \frac{\tan(\alpha_0)}{\cos\left(\frac{\alpha_0}{2}\right)} \sqrt{\gamma \sin(\alpha_0) + \cos(\alpha_0)}}{\frac{\overline{AO}}{2} \cdot \tan(\alpha_0)} = \frac{\sqrt{\gamma \sin(\alpha_0) + \cos(\alpha_0)}}{\cos\left(\frac{\alpha_0}{2}\right)} \quad (43)$$

C. Ellipse ratio of the elliptic cone during deformation

We also study a modified case of the elliptical cone, where the cone has an elliptical shape in the section normal to the cone axis. The ellipticity of the section is quantified with a parameter f , which is the ratio of the major to minor ellipse axis $f = r_\beta / r_\alpha$. We distinguish two cone angles α and β , which represent the largest and the smallest angle between the cone's surface in the sections that cut through the cones axis. α is the cone angle that is measured in the xz section. In the derivation, we use $r_\alpha = r$ and $r_\beta = fr_\alpha = fr$.

In such a case, R'_z is the same as in the previous analysis. The difference appears in the analysis of R'_y . We employ the ellipse equation, where $(\overline{ME}/r_\alpha)^2 + (R_y/r_\beta)^2 = 1$. We rearrange the equation as

$$(\overline{ME})^2 + \left(\frac{R_y}{f}\right)^2 = r^2 \quad (44)$$

thus

$$R'_y = f \cdot \sqrt{r^2 - \overline{ME}^2} \quad (45)$$

The derivation of the elliptical cone is analogous as in Appendix B, thus, the final formula is

$$R_{yz} = \frac{R'_y}{R_z} = f \frac{\sqrt{\gamma \sin(\alpha_0) + \cos(\alpha_0)}}{\cos\left(\frac{\alpha_0}{2}\right)} \quad (46)$$

D. Evolution of the two cone angles

After deformation, the point P moves to the initial position of A (cf. Figure A2 and Figure A3). The length $\overline{PB} = \overline{AB} = 2R_z$ does not change. We can use Figure A3B and C to calculate the evolution of cone angles α and β . The change of angle α can be described through the relation (Figure A3B)

$$\alpha = \tan^{-1} \frac{2R_z}{PO} \quad (47)$$

We substitute Eq. (10) and Eq. (34) and simplify the relation

$$\alpha = \tan^{-1} \frac{\overline{AO} \tan(\alpha_0)}{\overline{AO} [\gamma \cdot \tan(\alpha_0) + 1]} = \tan^{-1} \left[\frac{\sin(\alpha_0)}{\gamma \cdot \sin(\alpha_0) + \cos(\alpha_0)} \right] \quad (48)$$

The angle β can be described as

$$\beta = 2 \tan^{-1} \frac{r_\beta}{MO} \quad (49)$$

where (see Figure A3B)

$$\overline{MO} = \frac{r_\alpha}{\tan\left(\frac{\alpha}{2}\right)} \quad (50)$$

We find r_α using the relation

$$r_\alpha = \overline{KO} \cdot \sin\left(\frac{\alpha}{2}\right) \quad (51)$$

where $\overline{KO} = (\overline{PO} + \overline{BO})/2$ and $\overline{BO} = \overline{PO}/\cos(\alpha)$, thus

$$r_\alpha = \frac{\overline{PO}}{2} \left(1 + \frac{1}{\cos(\alpha)}\right) \cdot \sin\left(\frac{\alpha}{2}\right) = \frac{\overline{PO}}{2} \left(\frac{1 + \cos(\alpha)}{\cos(\alpha)}\right) \cdot \sin\left(\frac{\alpha}{2}\right) \quad (52)$$

We simplify the equation using the half angle formula for the cosine function and the double angle formula for the sine function

$$r_\alpha = \frac{\overline{PO}}{2} \cos\left(\frac{\alpha}{2}\right) \cdot \frac{\sin(\alpha)}{\cos(\alpha)} = \frac{\overline{PO}}{2} \cos\left(\frac{\alpha}{2}\right) \cdot \tan(\alpha) \quad (53)$$

We substitute $\overline{PO} = 2R_z/\tan(\alpha)$, so

$$r_\alpha = R_z \cos\left(\frac{\alpha}{2}\right) \quad (54)$$

We find r_β using the formula for the ellipse in the point E (Figure A3C)

$$\left(\frac{\overline{MC}}{r_\alpha}\right)^2 + \left(\frac{R'_y}{r_\beta}\right)^2 = 1 \quad (55)$$

and rearrange the formula

$$r_\beta = \frac{R'_y}{\sqrt{1 - \left(\frac{\overline{MC}}{r_\alpha}\right)^2}} = \frac{R'_y}{\sqrt{\frac{r_\alpha^2 - \overline{MC}^2}{r_\alpha^2}}} = \frac{R'_y \cdot r_\alpha}{\sqrt{r_\alpha^2 - \overline{MC}^2}} \quad (56)$$

We substitute Eq. (54) and the expression $\overline{MC} = \overline{KC} - r_\alpha$ into Eq. (56) and simplify it

$$r_\beta = \frac{R'_y \cdot R_z \cos\left(\frac{\alpha}{2}\right)}{\sqrt{r_\alpha^2 - \overline{MC}^2}} = \frac{R'_y \cdot R_z \cos\left(\frac{\alpha}{2}\right)}{\sqrt{r_\alpha^2 - (\overline{KC} - r_\alpha)^2}} = \frac{R'_y \cdot R_z \cos\left(\frac{\alpha}{2}\right)}{\sqrt{2r_\alpha \overline{KC} - (\overline{KC})^2}} \quad (57)$$

Expanding the expression under the square root and substituting the relation

$\overline{KC} = R_z/\cos(\alpha/2)$ and Eq. (54), we get

$$2r_\alpha \overline{KC} - (\overline{KC})^2 = 2R_z \cos\left(\frac{\alpha}{2}\right) \frac{R_z}{\cos\left(\frac{\alpha}{2}\right)} - \frac{R_z^2}{\cos^2\left(\frac{\alpha}{2}\right)} \quad (58)$$

We simplify the expression and use the double angle formula for the cosine function

$$\begin{aligned} 2r_\alpha \overline{KC} - (\overline{KC})^2 &= 2R_z^2 - \frac{R_z^2}{\cos^2\left(\frac{\alpha}{2}\right)} = R_z^2 \left[2 - \frac{1}{\cos^2\left(\frac{\alpha}{2}\right)} \right] = \\ &= \frac{R_z^2}{\cos^2\left(\frac{\alpha}{2}\right)} \left[2 \cos^2\left(\frac{\alpha}{2}\right) - 1 \right] = \frac{R_z^2}{\cos^2\left(\frac{\alpha}{2}\right)} \left[2 \cos^2\left(\frac{\alpha}{2}\right) - 1 \right] = \frac{R_z^2}{\cos^2\left(\frac{\alpha}{2}\right)} \cos(\alpha) \end{aligned} \quad (59)$$

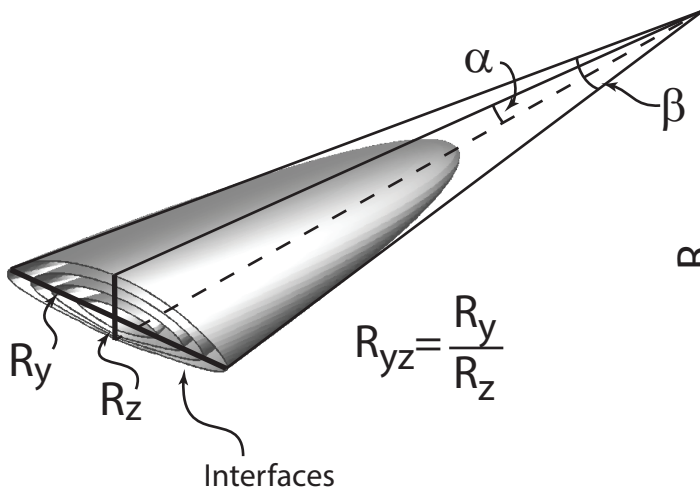
Thus

$$r_\beta = \frac{R'_y \cdot R_z \cos\left(\frac{\alpha}{2}\right)}{\sqrt{\frac{R_z^2}{\cos^2\left(\frac{\alpha}{2}\right)} \cos(\alpha)}} = \frac{R'_y \cdot R_z \cos\left(\frac{\alpha}{2}\right)}{\frac{R_z}{\cos\left(\frac{\alpha}{2}\right)} \sqrt{\cos(\alpha)}} = \frac{R'_y \cos^2\left(\frac{\alpha}{2}\right)}{\sqrt{\cos(\alpha)}} \quad (60)$$

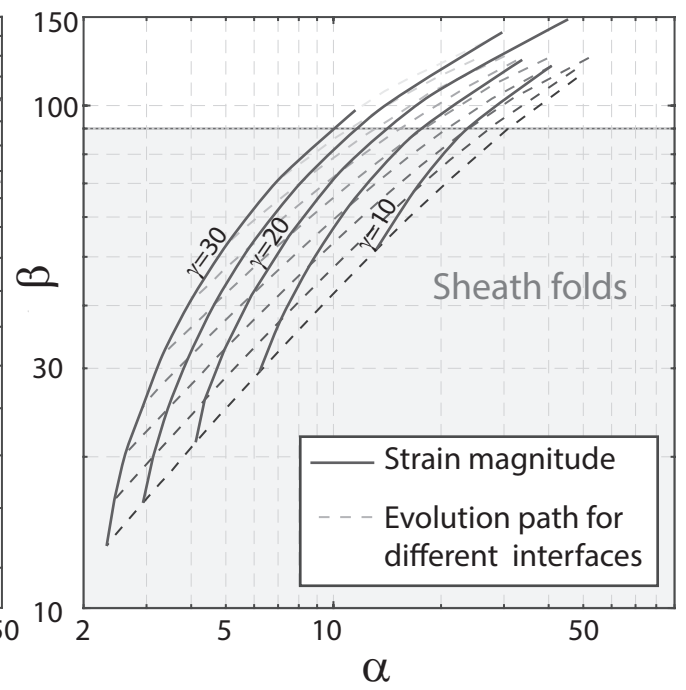
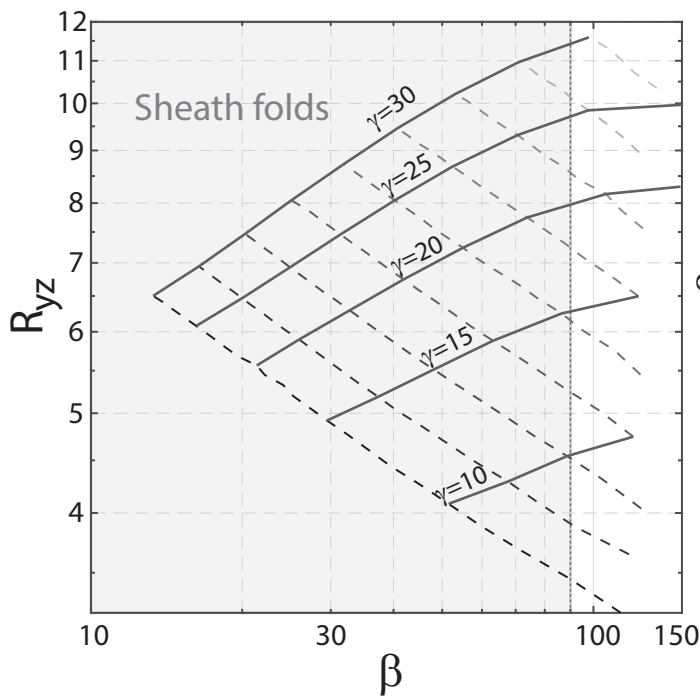
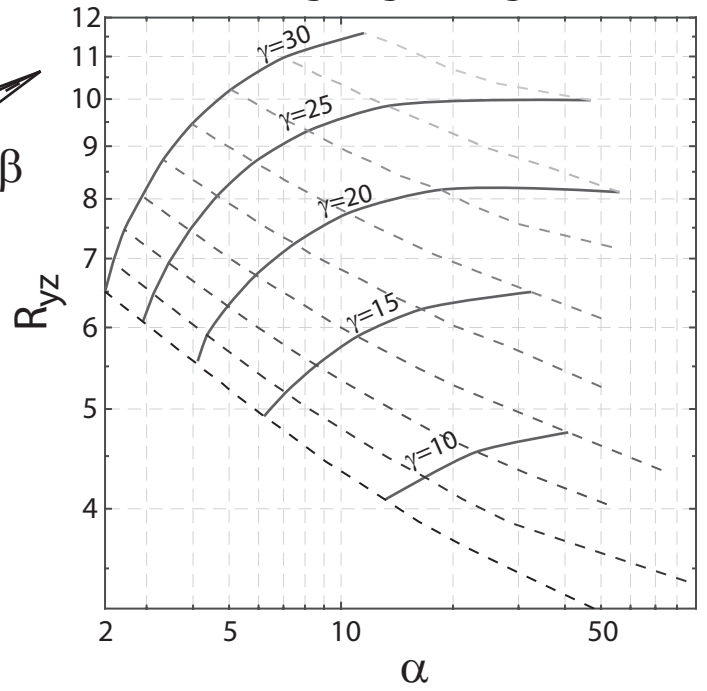
Finally, we substitute Eq. (60) and Eq. (50) into Eq. (49) and simplify it

$$\beta = 2 \tan^{-1} \left[\frac{\frac{R'_y \cos^2\left(\frac{\alpha}{2}\right)}{\sqrt{\cos(\alpha)}}}{\frac{R_z \cos\left(\frac{\alpha}{2}\right)}{\tan\left(\frac{\alpha}{2}\right)}} \right] = 2 \tan^{-1} \left[\frac{R'_y}{R_z} \frac{\sin\left(\frac{\alpha}{2}\right)}{\sqrt{\cos(\alpha)}} \right] \quad (61)$$

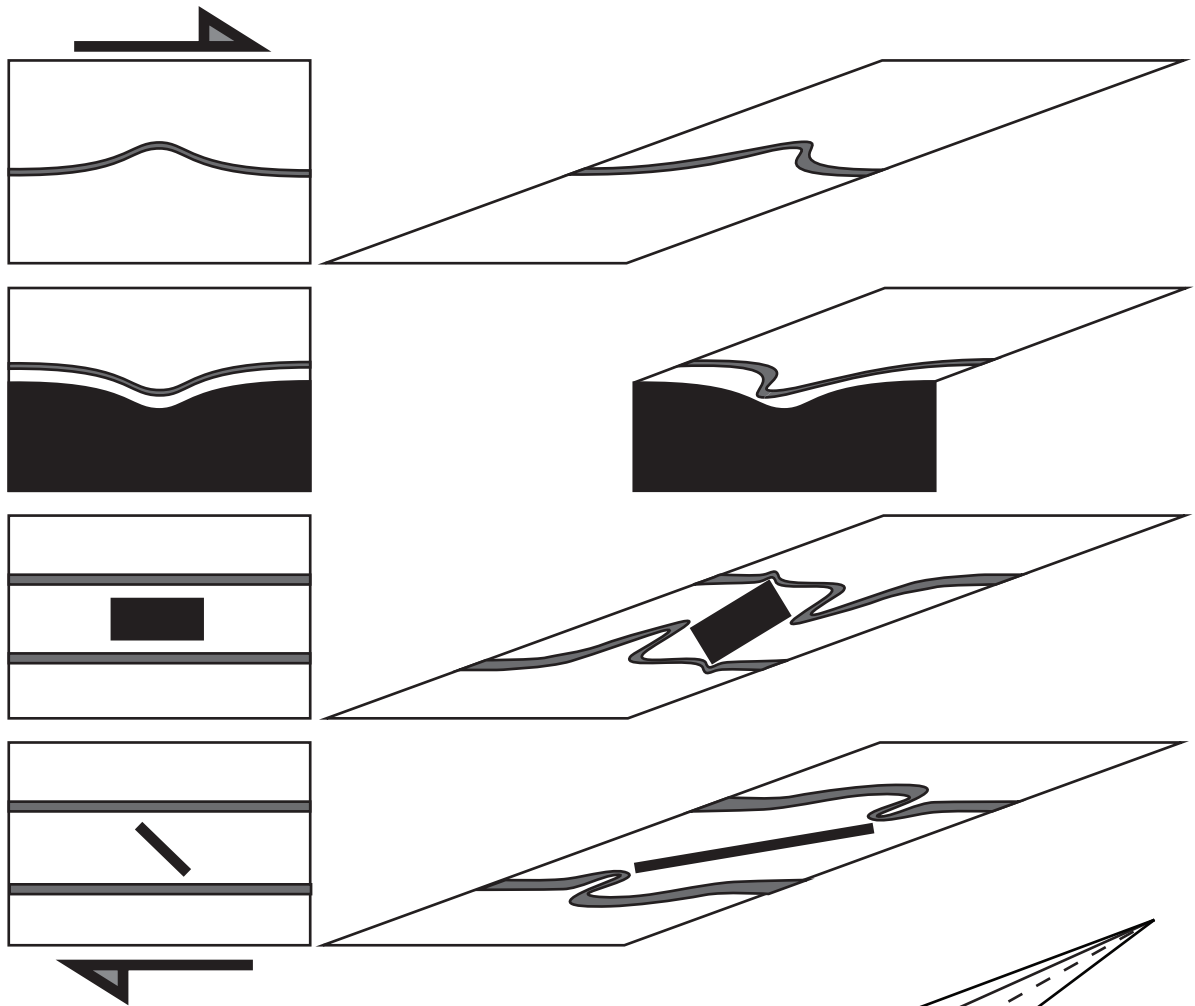
Sheath fold shape parameters



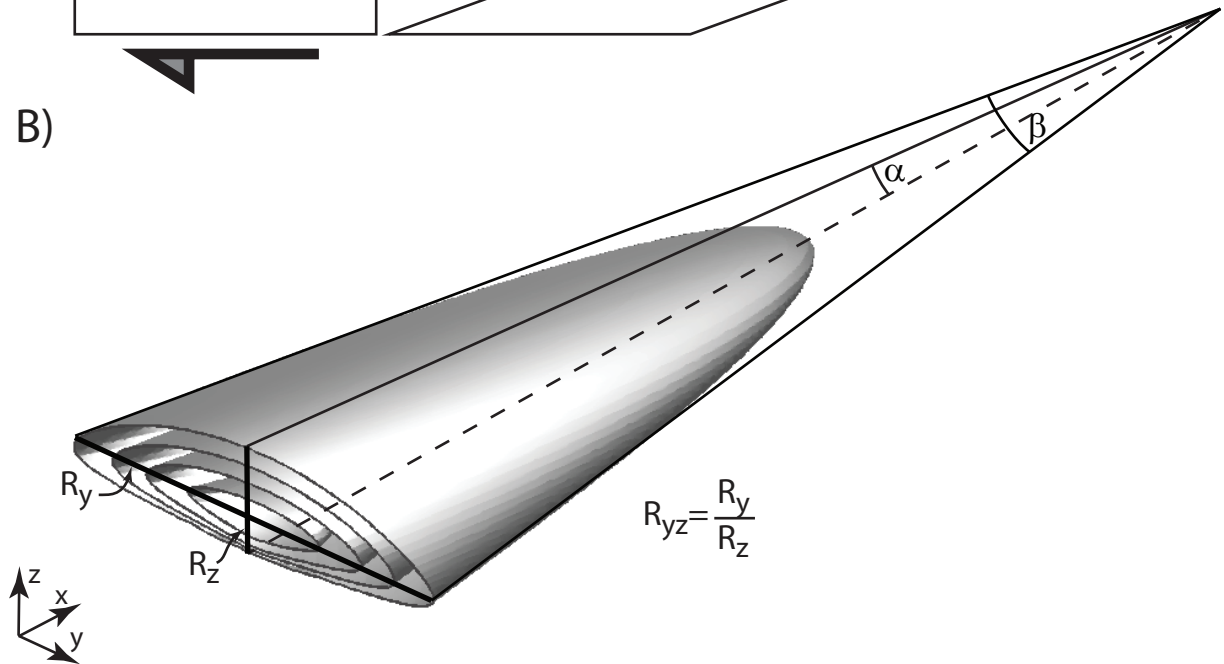
Strain gauge diagrams

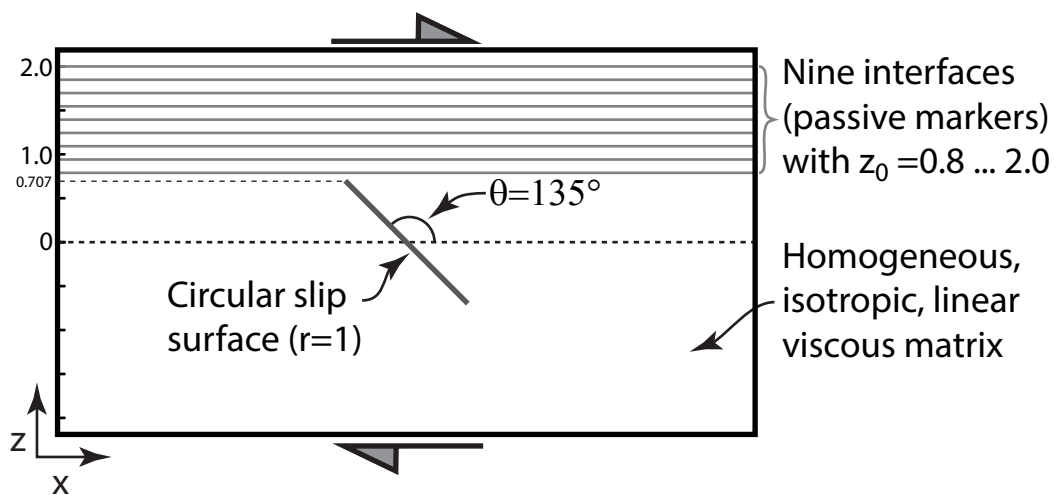


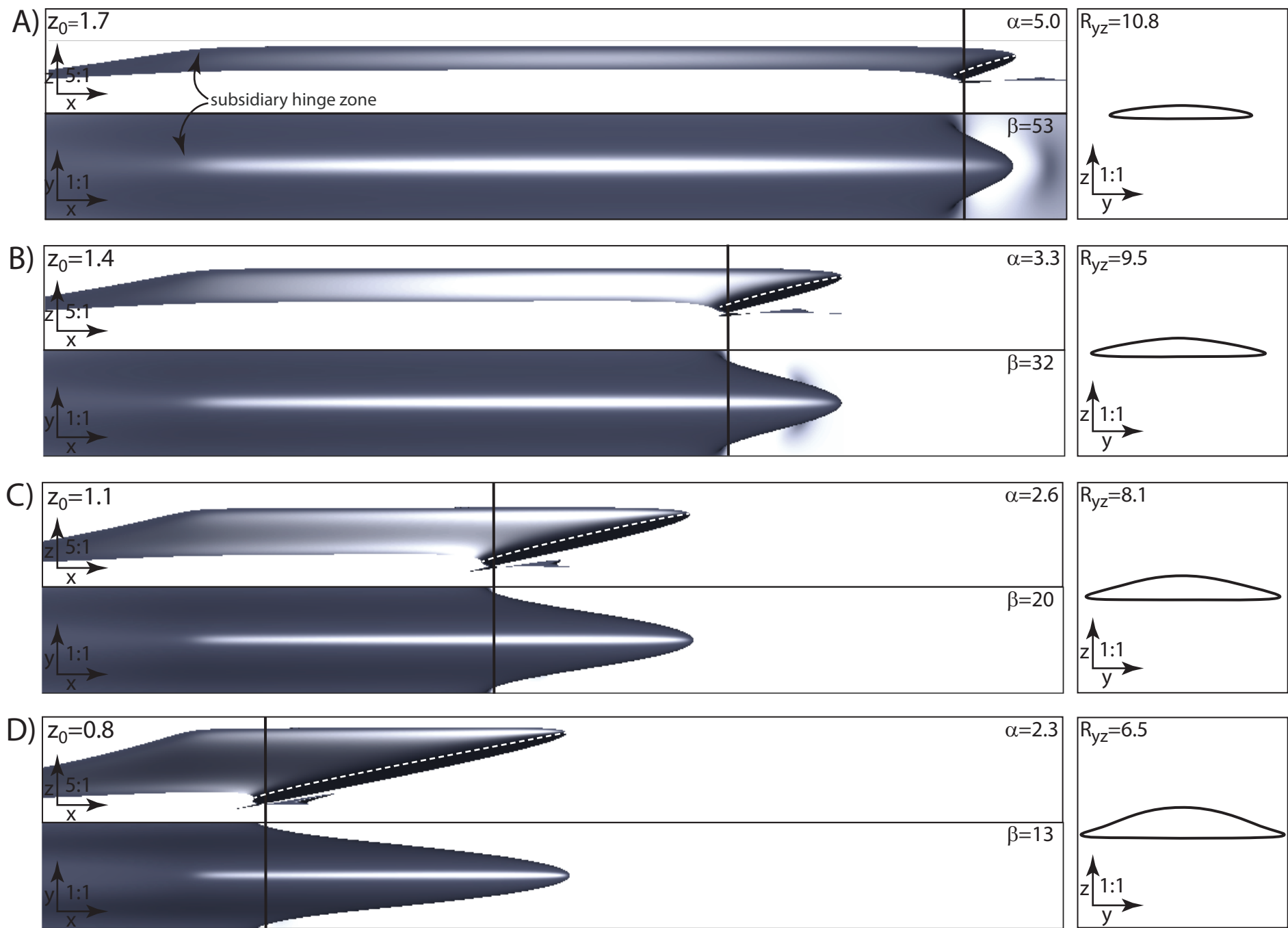
A)

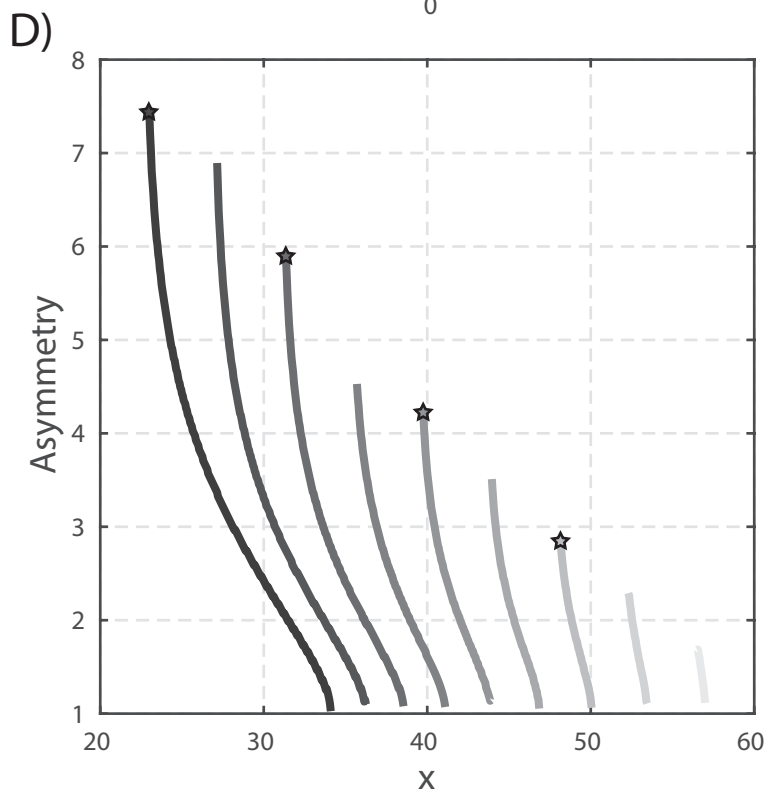
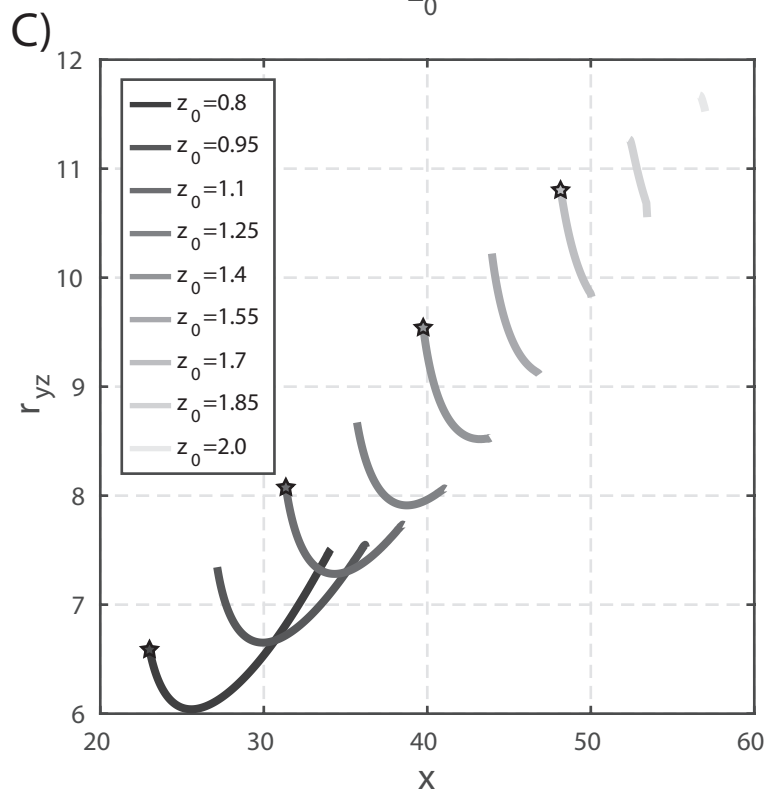
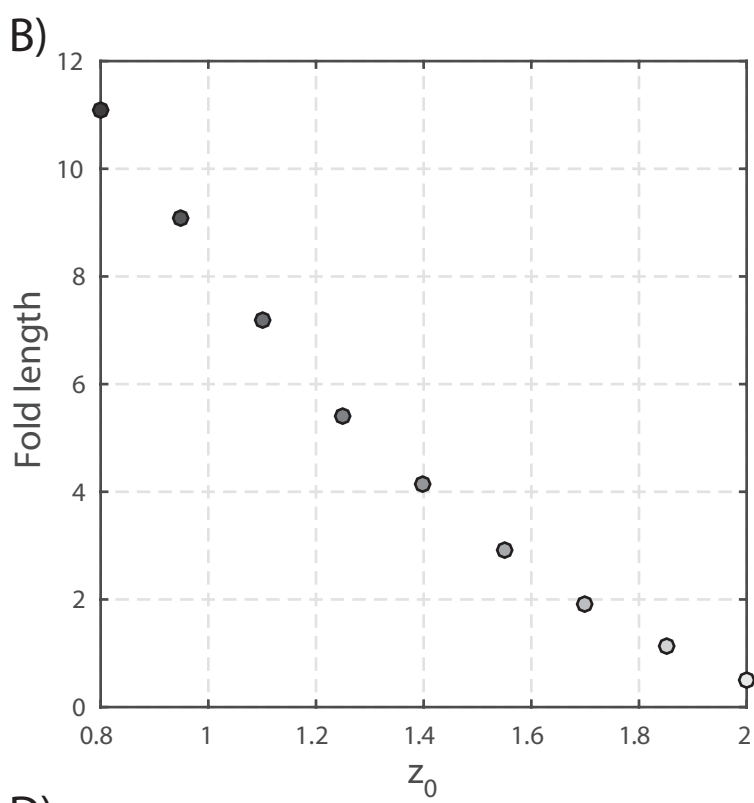
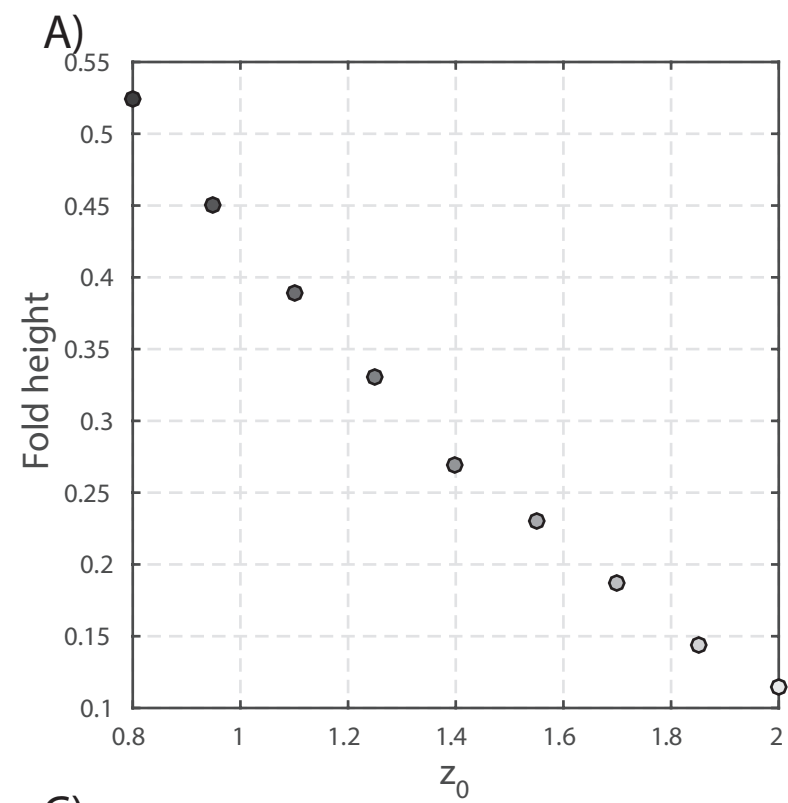


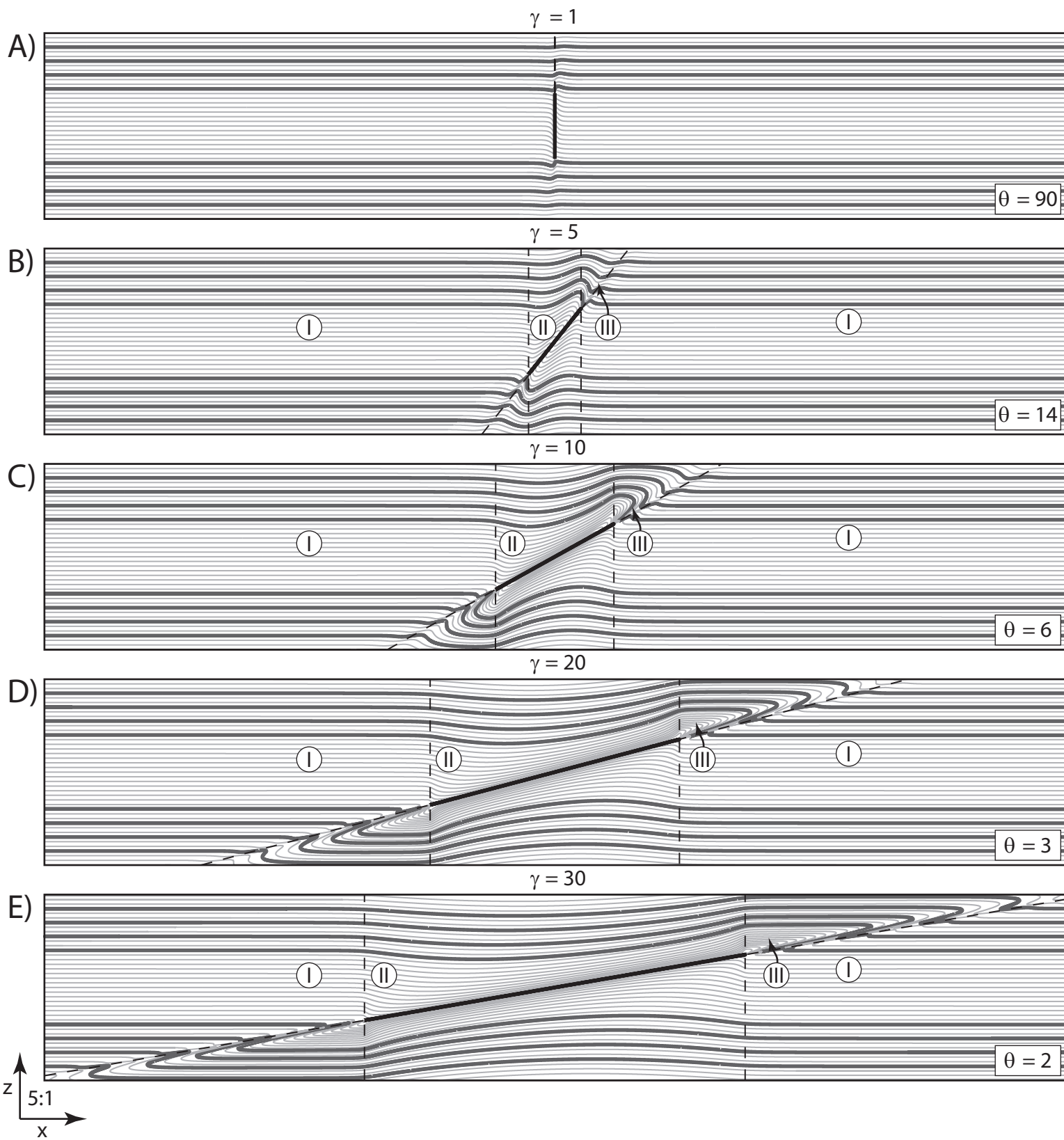
B)

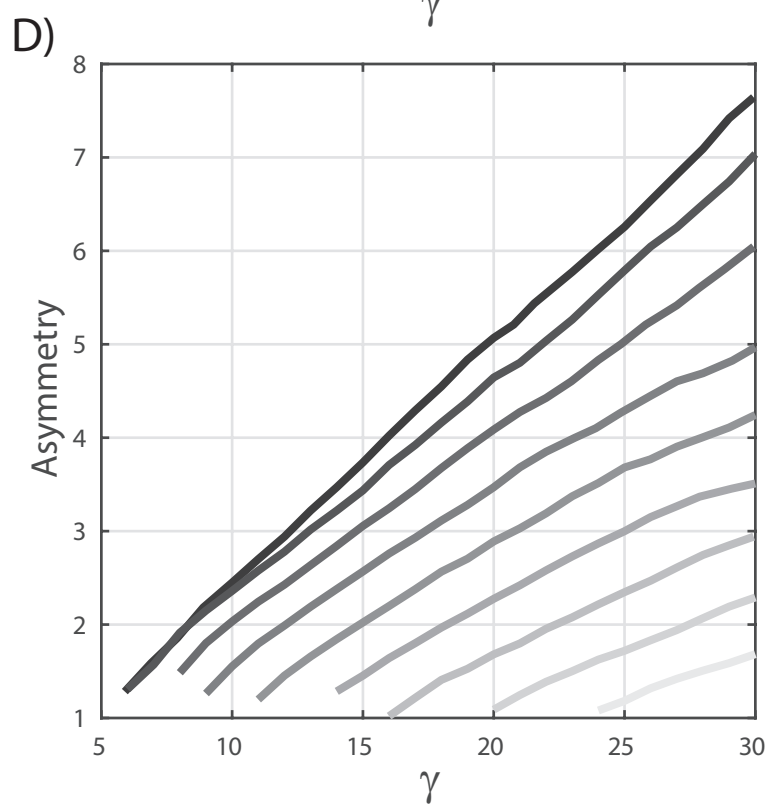
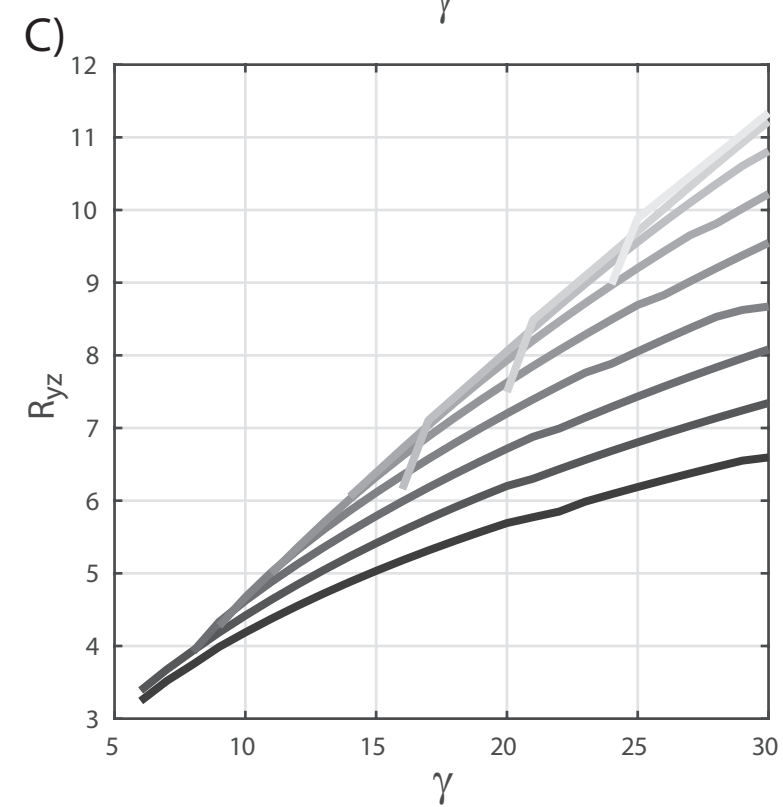
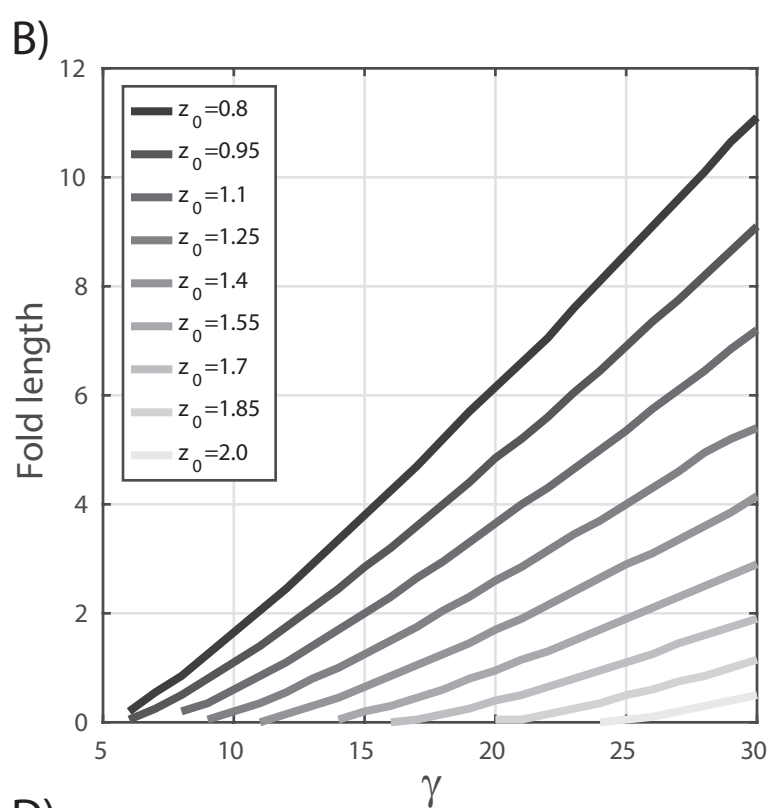
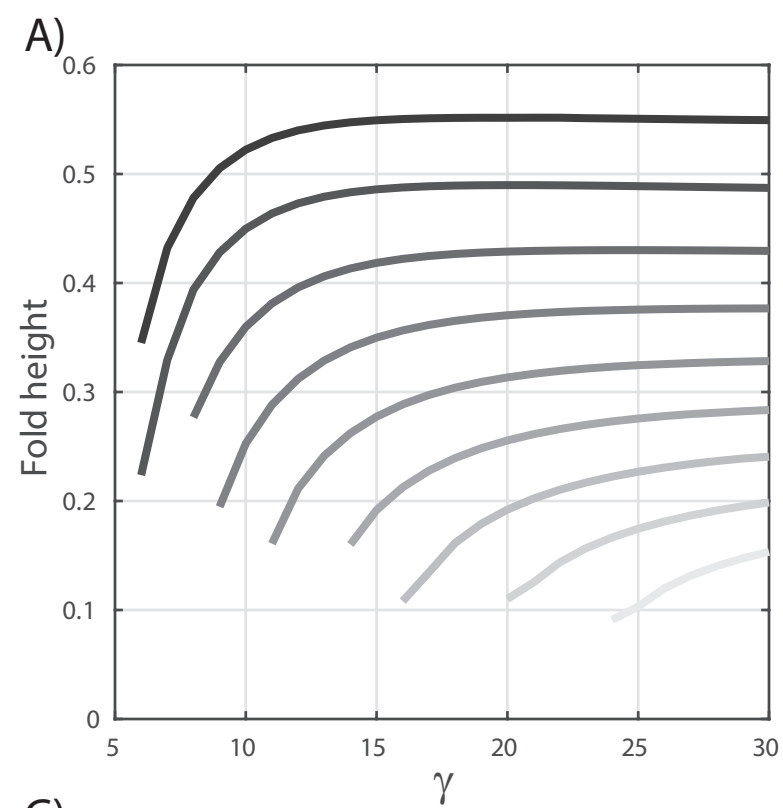


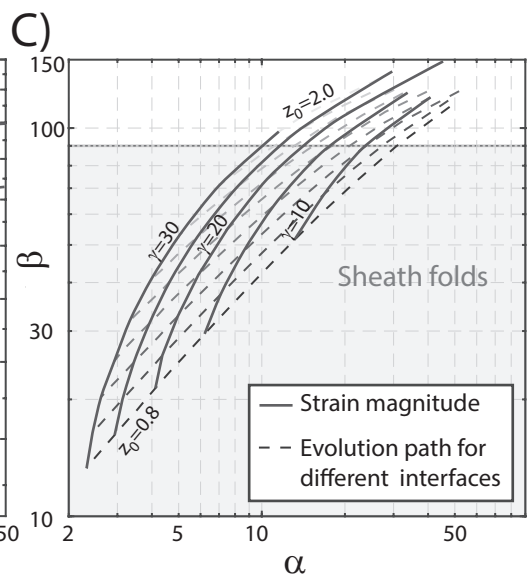
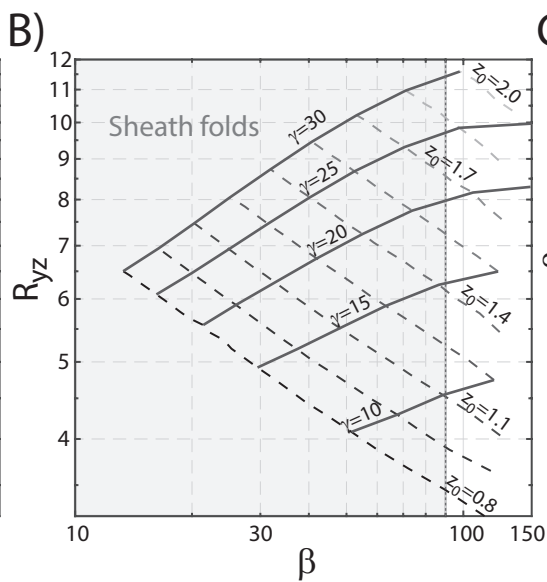
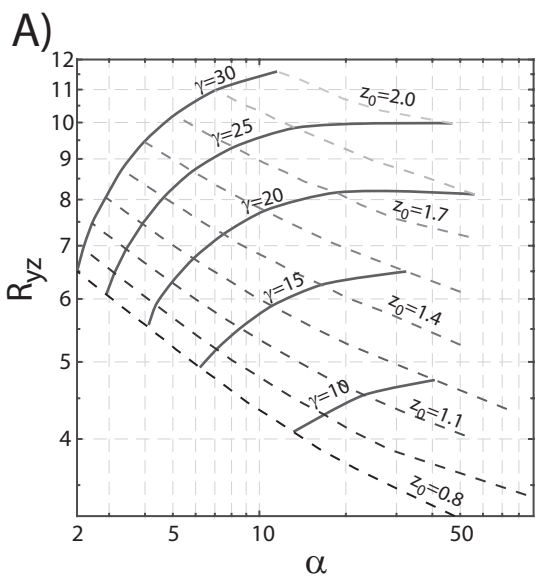


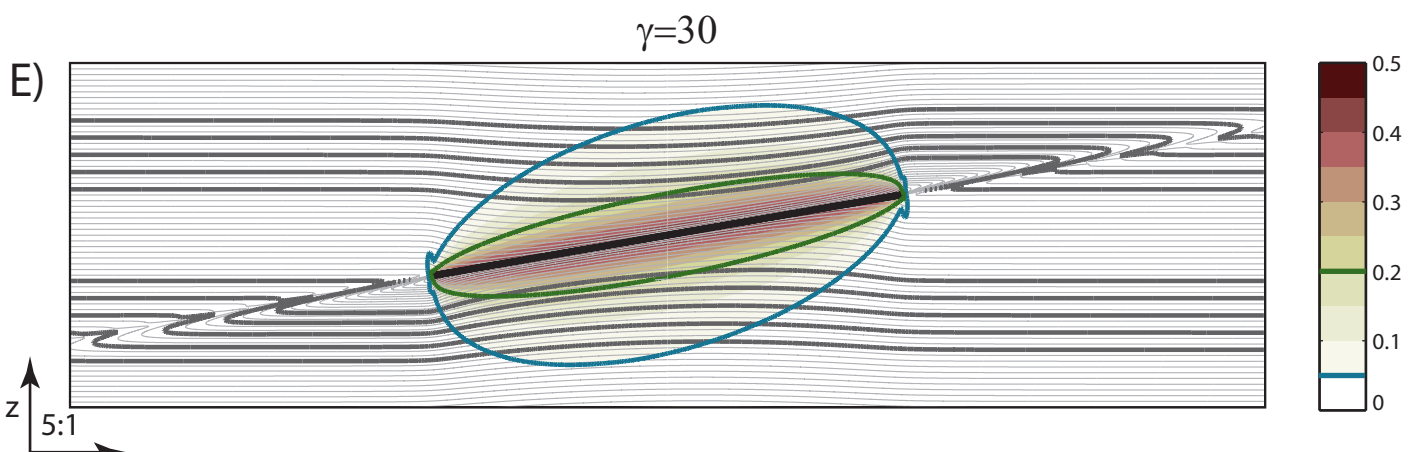
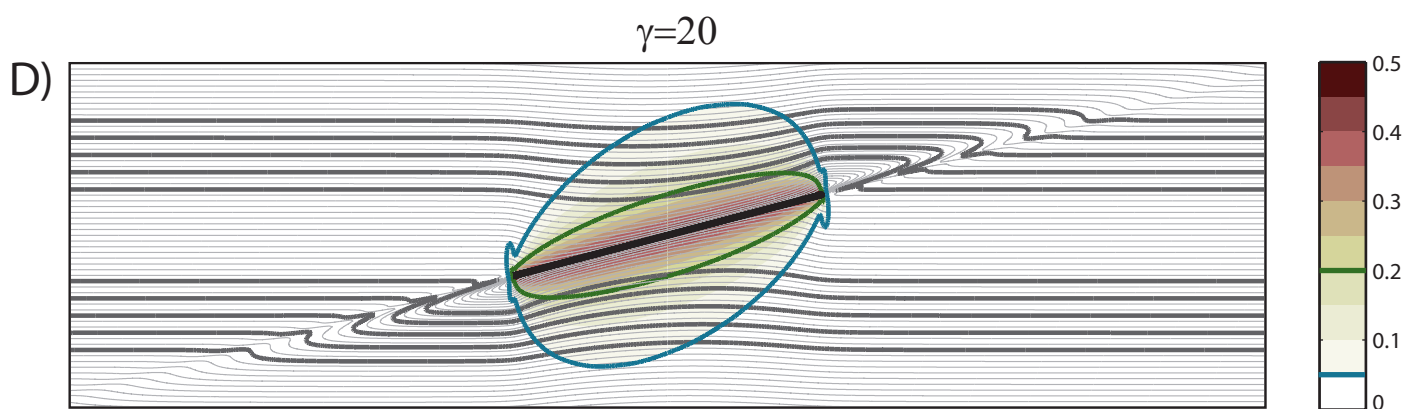
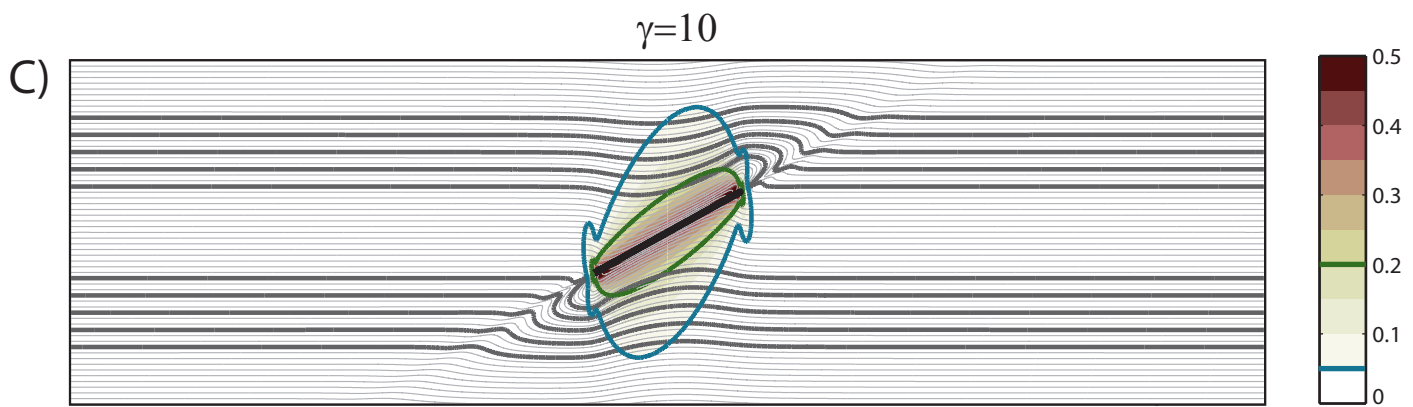
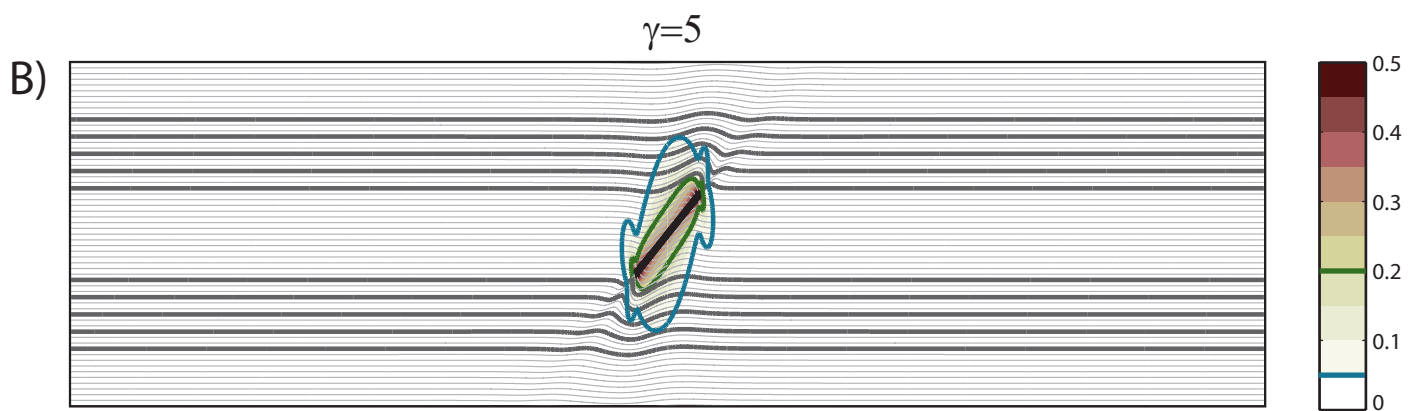
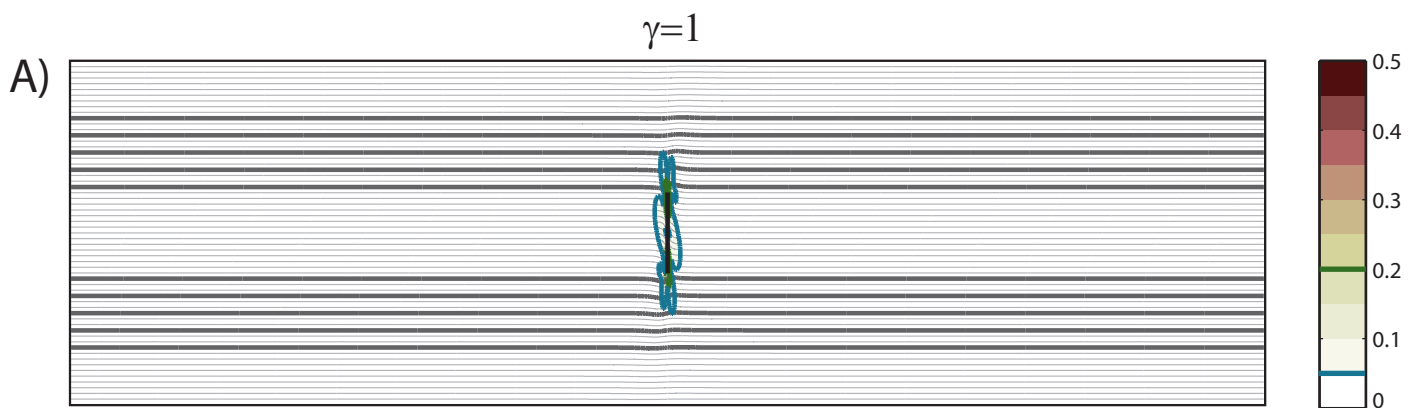


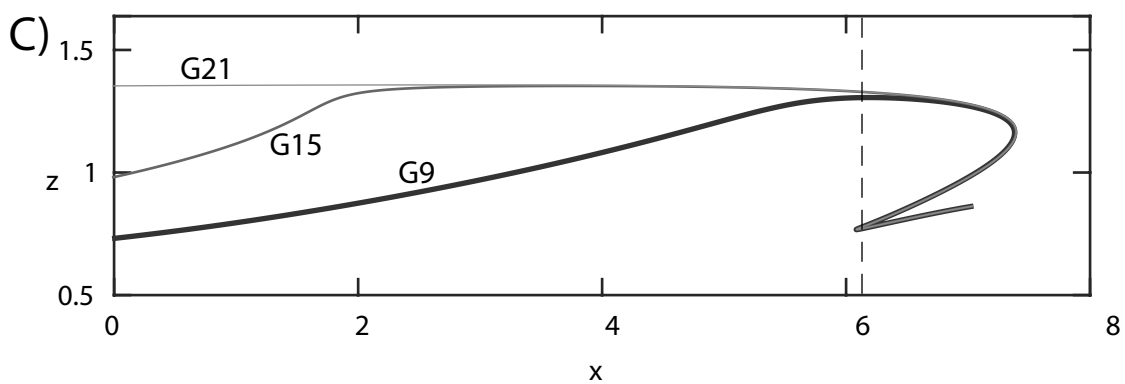
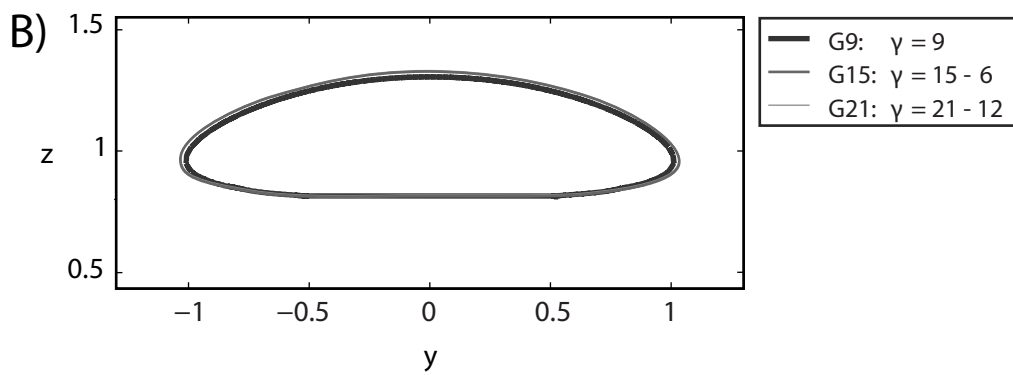
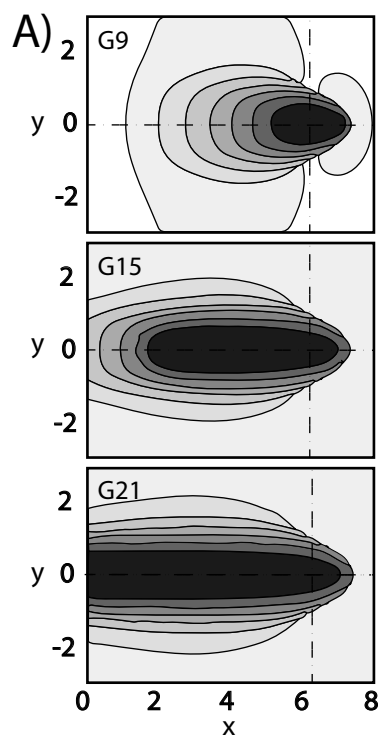




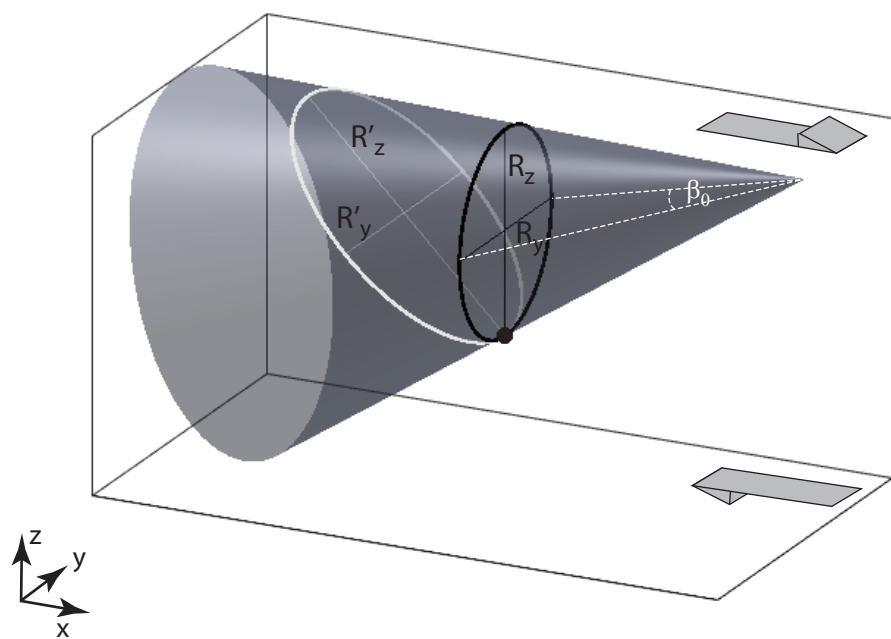




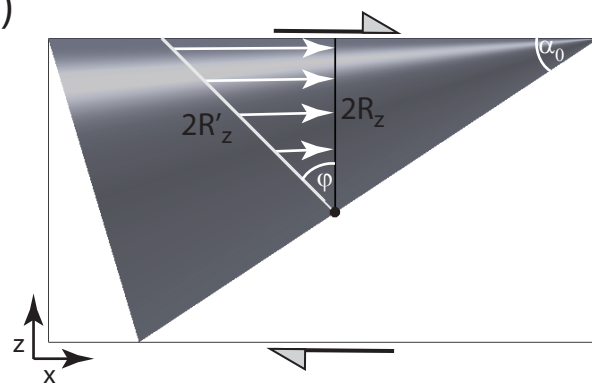




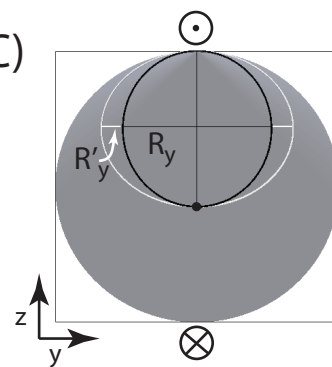
A)

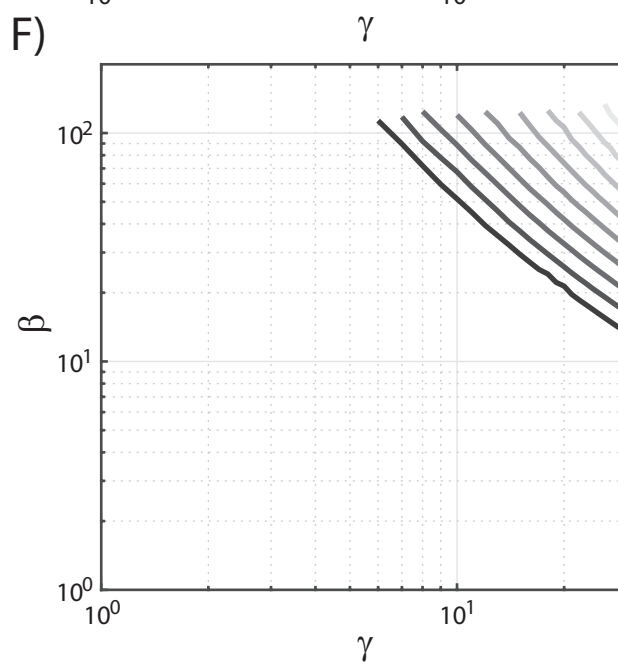
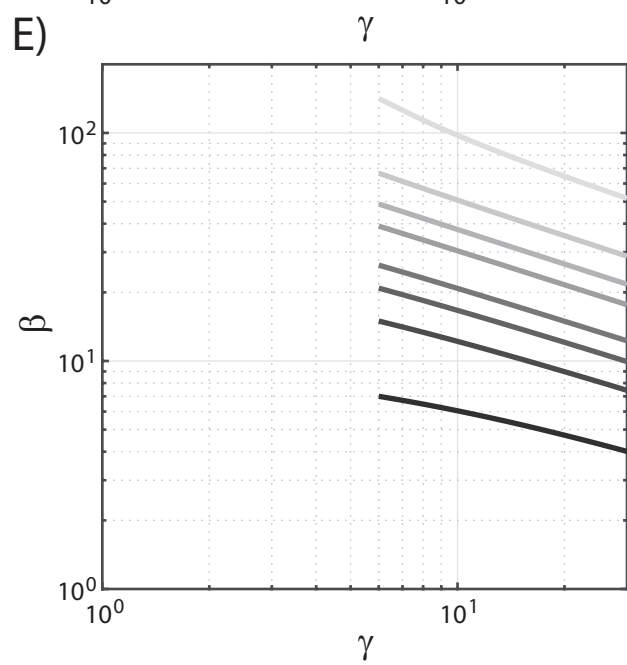
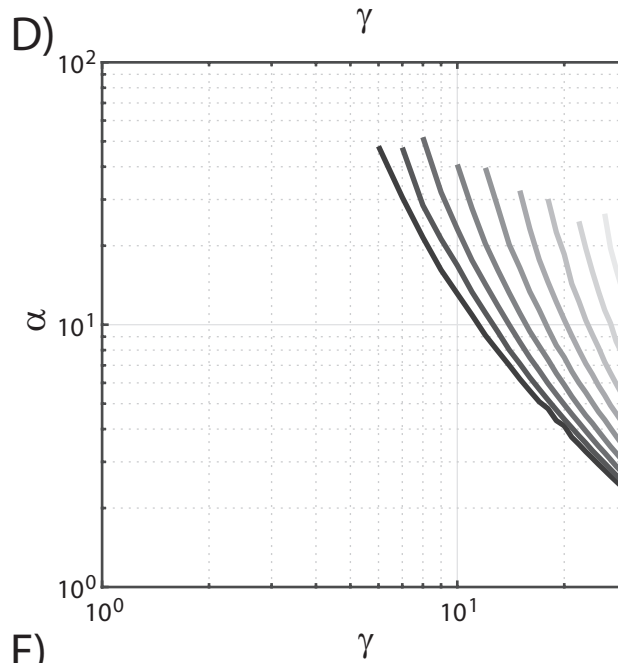
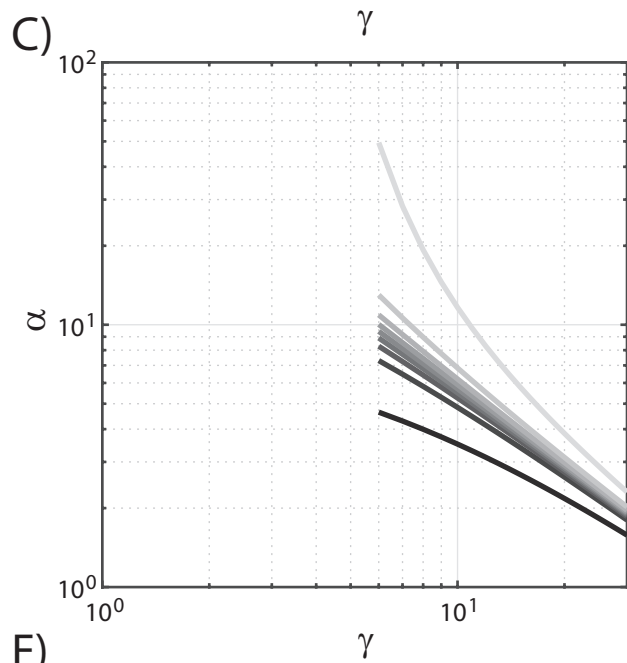
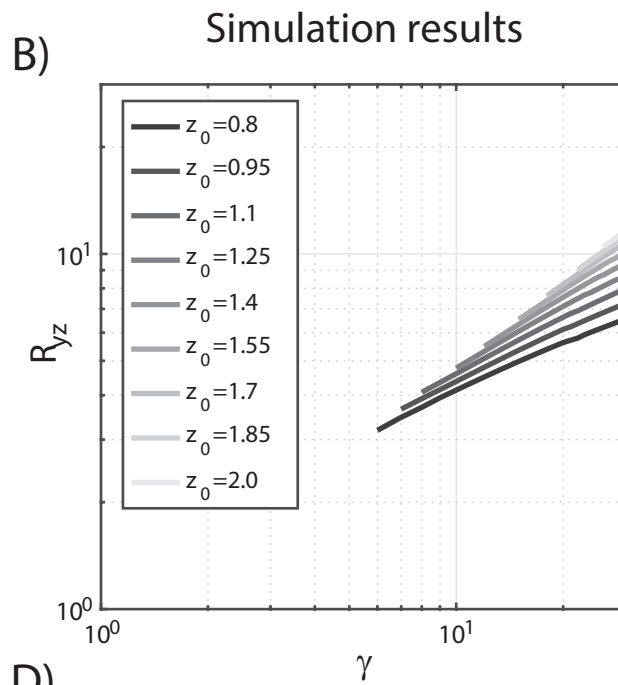
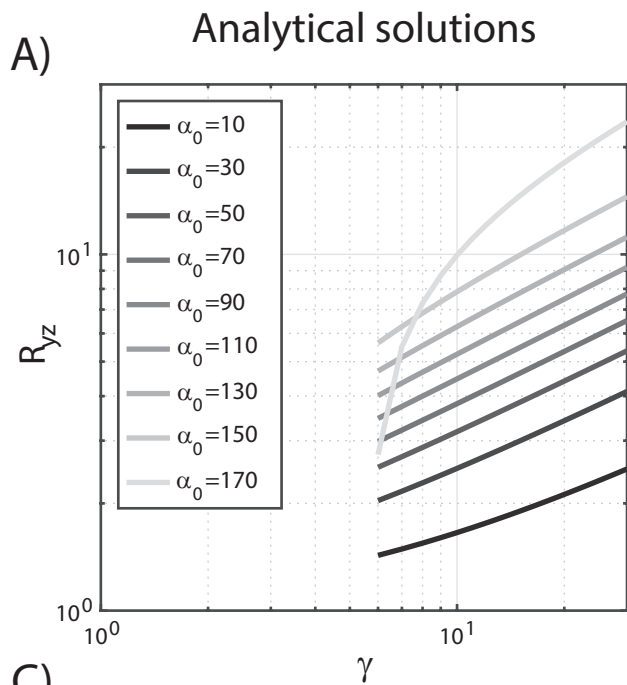


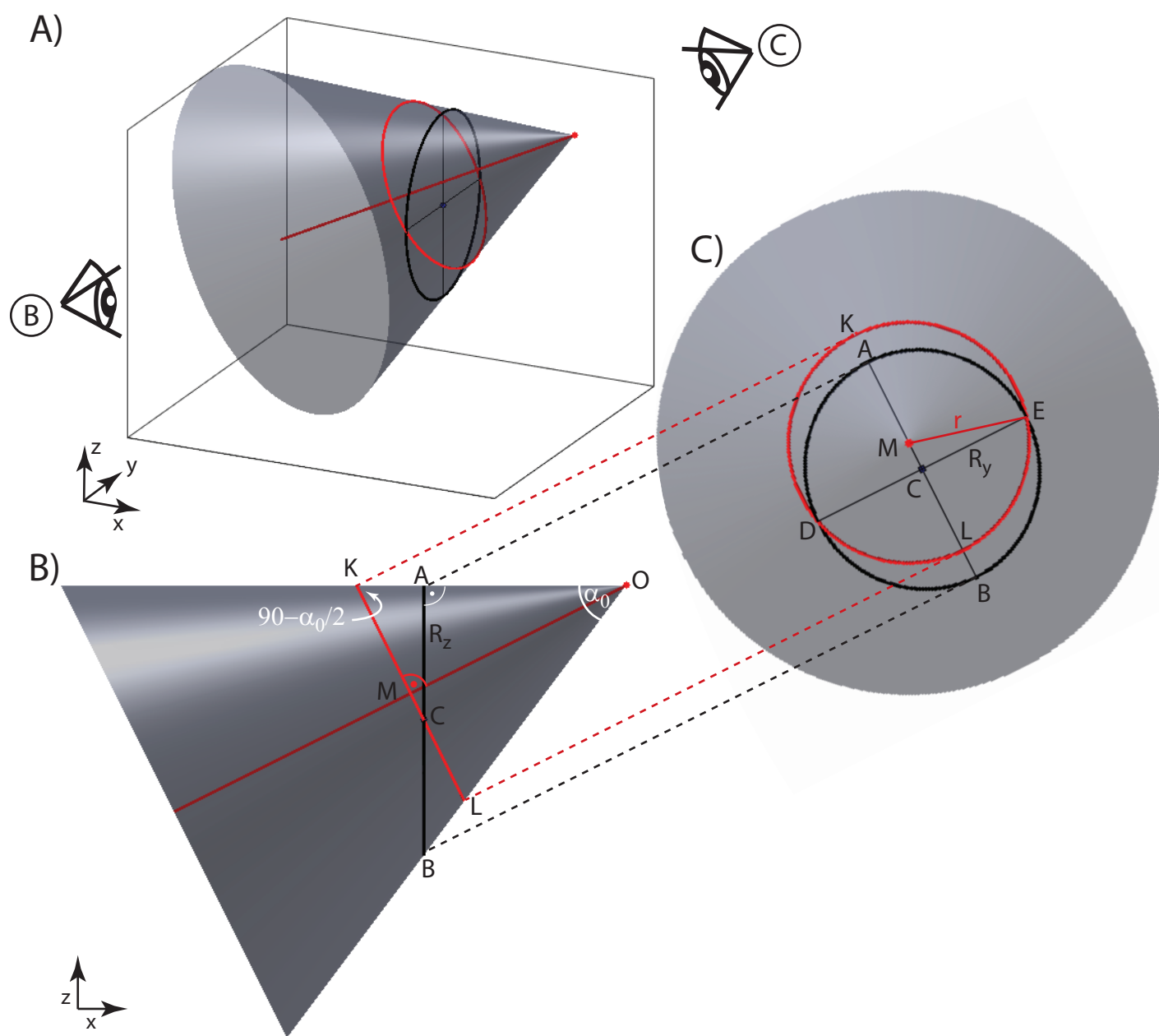
B)

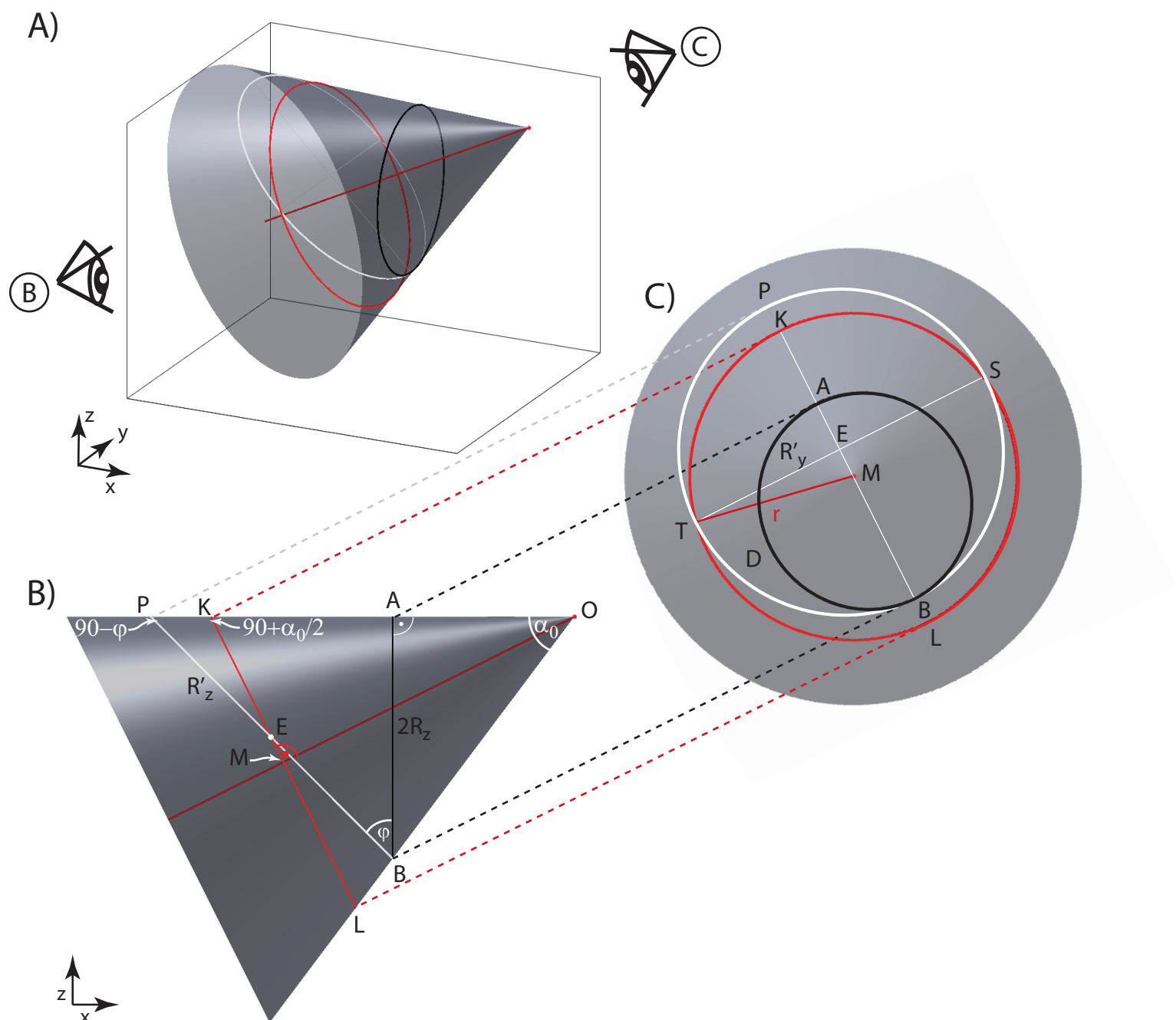


C)

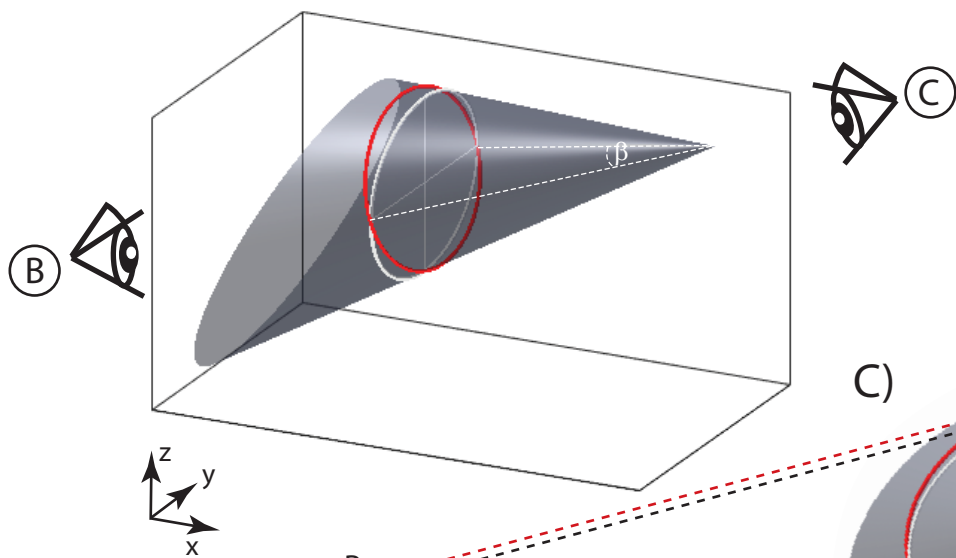




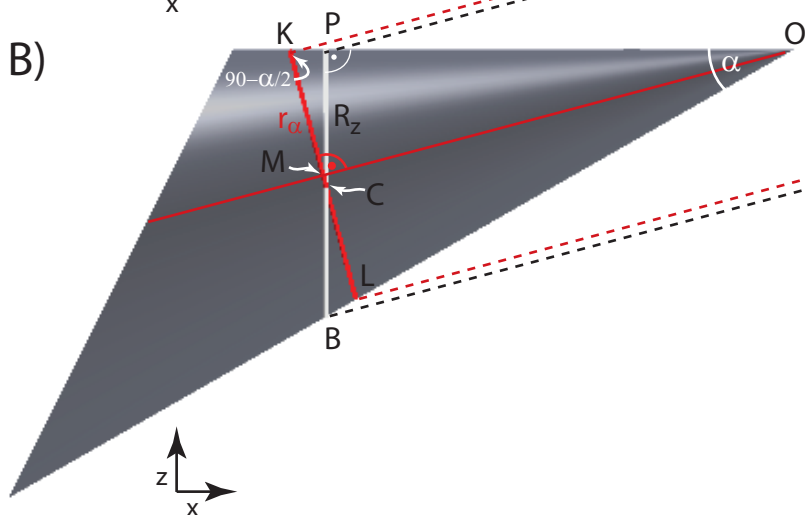




A)



B)



C)

